*Published online 20 February 2023*

*Nucleic Acids Research, 2023, Vol. 51, No. 8* ***3631–3649***
*https://doi.org/10.1093/nar/gkad072*

# PBRM1 bromodomains associate with RNA to facilitate chromatin association

**Saumya M. De Silva[1,2,†], Alisha Dhiman[3,†], Surbhi Sood[3], Kilsia F. Mercedes[1], William J. Simmons[1], Morkos A. Henen[1], Beat Vögeli[1], Emily C. Dykhuizen[3,*] and Catherine A. Musselman[1,2,*]**

[1]Department of Biochemistry and Molecular Genetics, University of Colorado Anschutz Medical Campus, Aurora, CO 80045, USA, [2]Department of Biochemistry, University of Iowa, Iowa City, IA 52242, USA and [3]Department of Medicinal Chemistry and Molecular Pharmacology, Purdue University, West Lafayette, IN 47907, USA

Received February 14, 2022; Revised January 03, 2023; Editorial Decision January 22, 2023; Accepted February 16, 2023

## ABSTRACT

**PBRM1 is a subunit of the PBAF chromatin remodeling complex, which is mutated in 40–50% of clear cell renal cell carcinoma patients. It is thought to largely function as a chromatin binding subunit of the PBAF complex, but the molecular mechanism underlying this activity is not fully known. PBRM1 contains six tandem bromodomains which are known to cooperate in binding of nucleosomes acetylated at histone H3 lysine 14 (H3K14ac). Here, we demonstrate that the second and fourth bromodomains from PBRM1 also bind nucleic acids, selectively associating with double stranded RNA elements. Disruption of the RNA binding pocket is found to compromise PBRM1 chromatin binding and inhibit PBRM1-mediated cellular growth effects.**

## INTRODUCTION

Eukaryotic DNA is packaged into the cell nucleus in the form of chromatin. At its most basic level chromatin is made up of repeats of the basic subunit, the nucleosome (1,2). Each nucleosome is composed of ∼147 base pairs (bp) of DNA, wrapped around an octamer of histone proteins containing two copies each of H2A, H2B, H3 and H4 (3). Spatial and temporal modulation of chromatin structure is critical in all DNA-templated processes. This is facilitated by several mechanisms including ATP-dependent remodeling of the nucleosome by multi-subunit protein complexes known as chromatin remodelers (4,5). The action of the remodelers is tightly regulated by a variety of factors including complex composition and post-translational modification (PTM) of the histone proteins (6), and can also be modulated by association with non-coding RNAs (ncRNA) (7,8). Together, these factors stabilize complexes at specific regions of chromatin as well as modulate their activity.

There are several families of chromatin remodeling complexes, including SWI/ SNF, which was first identified in yeast (9). In humans, the SWI/SNF family of remodelers exists primarily as cBAF (hSWI/SNF-A) (10–12), PBAF (hSWI/SNF-B) (13,14), and GBAF (ncBAF) (15,16). PBAF is defined by the exclusive incorporation of ARID2, BRD7, PHF10, and PBRM1 (also known as BAF180 or PB1) (17,18). SWI/SNF subunits are mutated in ∼20% of human tumors (19), with the PBRM1 subunit mutated primarily in 40–50% of clear cell renal cell carcinomas (ccRCC) (20,21). PBRM1 is a bona fide tumor suppressor in ccRCC in the context of VHL deletion (22–24); however, in other cancer contexts, it is oncogenic and a proposed therapeutic target (25–27). Though its best characterized function is in DNA damage repair (28), its role in oncogenesis is also associated with transcriptional activity (29,30), at least in part through the activation of stress-response genes (31,32).

PBRM1 contains several chromatin-binding domains and is thought to function largely as a chromatin targeting subunit of PBAF. This includes six bromodomains (BDs), two bromo-adjacent homology (BAH) domains, and a high mobility group (HMG) domain (Figure 1A) (14,33). The HMG domain of PBRM1 has been shown to interact with nucleosomal DNA (10,34,35), whereas the BAH domains are thought to be protein-protein interaction domains (36), with one recent study implicating them as readers for methylated lysine 40 of α-tubulin on spindle microtubules (37). Bromodomains (BDs) are ∼100aa four-helix bundles that associate with acetylated histones (38–40). The BDs of PBRM1 are structurally well conserved despite substantial differences in sequence (Supplementary Figure S1). Studies on the six BDs reveal that they cooperate in binding to nucleosomes containing histone H3 acetylated at lysine

*To whom correspondence should be addressed. Tel: +1 303 724 3208; Email: catherine.musselman@cuanschutz.edu
Correspondence may also be addressed to Emily C. Dykhuizen. Tel: +1 765 494 4706; Email: edykhui@purdue.edu
†The authors wish it to be known that, in their opinion, the first two authors should be regarded as Joint First Authors.

14 (H3K14ac) (41–43). From several different assays BD2 and BD4 appear to be most important for robust H3K14ac binding with BD1, BD5 and BD6 enhancing activity, while BD3 has been proposed to attenuate it. The acetyl-lysine binding activity of the BDs, particularly BD2 and BD4, is critical for cell proliferation and PBRM1-mediated gene expression (42–44).

Recently, a subset of BDs has been discovered to associate with DNA or RNA, in addition to binding acetylated histone tails (45–50). The BRG1 and hBRM BDs as well as BDs in BRD2, BRD3, BRD4 and BRDT interact with free and nucleosomal DNA. In addition, BRD3 and BRD4 BDs associate with non-coding RNA (ncRNA) (49,50). The binding of BDs to DNA has largely been found not to enhance affinity for histone peptides, though interestingly it was recently found that for BRD4 BD2 binding to DNA blocked histone peptide binding (51). However, for the BRD4 BD1–BD2 cassette, RNA binding was found to enhance association with acetylated histone tails (47), though the mechanism for this is unknown.

Morrison et. al predicted that ∼30% of known BDs will bind to nucleic acids, and this includes BD2, BD3, BD4 and BD5 of PBRM1 (46). Here we demonstrate that PBRM1 BD2 and BD4 selectively associate with double-stranded RNA elements, this binding enhances the association with H3K14ac peptides, and the nucleic acid binding activity of these domains is important for PBRM1-mediated chromatin association and cell proliferative effects.

## MATERIALS AND METHODS

### Cloning and expression of PBRM1 bromodomains and bromodomain mutants

Codon optimized plasmids encoding the individual His-tagged PBRM1 bromodomain constructs were received from Nicola Burgess-Brown (Addgene plasmid numbers 38999, 39013, 39027, 39028, 39030, 39103). Individual BDs were as follows: BD1 (residues 43–156), BD2 (residues 178–291), BD3 (residues 388–494), BD4 (residues 496–637), BD5 (residues 645–766), BD6 (residues 774–917). Bromodomain mutants were generated using the Q5 site-directed mutagenesis kit (New England Biolabs) and each mutation was confirmed through DNA sequencing. All constructs were expressed in *Escherichia coli* BL21 DE3 cells (New England Biolabs, Ipswich, MA). Cells were grown in LB media (VWR) at 37°C in the presence of 50 μg/l kanamycin (VWR). When the cultures reached an $OD_{600}$ ∼1–1.2, cells were harvested at 4000 rpm for 15 min at 22°C. Cell pellets were resuspended in M9 minimal media (at 1:4 ratio of M9:LB) containing 1g/l $^{15}N$ ammonium chloride and 5g/l D-glucose or 4g/l $^{13}C$-D-glucose, as well as vitamins (Centrum, 5 ml of 1 tablet resuspended in 50 ml water). After resting for an hour, cells were induced with 1 mM IPTG and allowed to grow at 18°C for 18 h. Cells were harvested by centrifugation at 6000 rpm for 20–30 min at 4°C. Cell pellets were flash frozen in liquid $N_2$ and stored at −80°C.

### Protein purification

Cell pellets were resuspended in lysis buffer containing 50 mM potassium phosphate at pH 7.0, 500 mM KCl, 2 mM DTT, 0.5% Triton X-100, 0.5 mg/ml lysozyme, DNAse I (RNase free, Thermo Fisher), and an EDTA-free protease inhibitor cocktail tablet (Roche mini tablets). Cells were lysed via sonication and the cell lysate was cleared by centrifugation at 15 000 rpm at 4°C for 1 h. The soluble fraction was loaded onto a column packed with Ni(II)-nitriloriacetic acid agarose (Qiagen) pre-equilibrated in 100 ml of binding buffer (50 mM potassium phosphate at pH 7.0, 50 mM KCl, 2 mM DTT and 5 mM imidazole), then eluted with 200–500 mM imidazole and dialyzed against dialysis buffer to remove imidazole. The His tag was cleaved using TEV protease at 18°C for 4–6 h. Cleaved protein was further purified by fast protein liquid chromatography (FPLC) using a Source-S cation-exchange column (GE Healthcare) (low salt buffer with 50 mM potassium phosphate at pH 7.0, 50 mM KCl, 2 mM DTT, 2 mM EDTA and high salt buffer with 50 mM potassium phosphate at pH 7.0, 1M KCl, 2 mM DTT, 2 mM EDTA). This was followed by purification over a Superdex 75 size-exclusion column (GE Healthcare). The final buffer was 50 mM potassium phosphate at pH 7.0, 50 mM KCl, 2 mM DTT, 2 mM EDTA. For PBRM1 BD2 and BD4, there was incomplete cleaving of the His tag. Therefore, after cleavage the protein was run over a Ni(II)-nitriloriacetic acid agarose column again before the cation exchange step to remove the uncleaved species.

### Electrophoretic mobility shift assays (EMSAs)

601 DNA was purified as previously described (52). Samples for EMSAs were prepared by mixing 1.5 pmol of Widom 601 DNA with varying amounts of individual bromodomains to reach final molar ratios of DNA:protein of 1:0, 1:1, 1:4, 1:6, 1:10, 1:15, 1:20 and 1:30 in a final buffer containing 50 mM potassium phosphate at pH 7.0, 10 mM KCl, 2 mM DTT, 2 mM EDTA and 5% v/v sucrose for gel loading purposes. While the samples were equilibrating on ice for an hour 5% 75:1 acrylamide:bisacrylamide native gel was pre-run in 0.2X TBE buffer on ice at 4°C for 30 min at 120 V. The samples were run on ice at 4°C for 50 min at 125 V. Gels were stained with ethidium bromide or SYBR green (Fisher) and visualized using an ImageQuant LAS 4000 imager/BIO-RAD Gel Doc imager.

### Preparation of oligonucleotides

DNA and RNA oligonucleotides for NMR experiments were obtained from Integrated DNA Technologies (IDT, Inc.). The following sequences were used: dsDNA (5' CGTAGACAGCT 3' and 5' AGCTGTCTACG 3'), ssDNA (5' CGTAGACAGCT 3'), dsRNAI (5' GCGUAGACAGCUGUUCGCAGCUGUCUACGC 3'), dsRNAII (5' GGCAUCGUGCUUC GGCACGAUGCC 3'), dsRNAIII (5' GGCAUCGUGCAUCAGAAUGGCACGAUGCC 3'), dsRNA IV (5' GGCAUCGUGC 3' and 5' GCACGAUGCC 3'), ssRNAI (5' UUUUUUUUUUUUU 3'), ssRNAII (5' ACACACACACACA 3'). To anneal the DNA, single stranded oligos were mixed at a 1:1 molar ratio, heated to 95°C for 5 min and allowed to cool overnight to room temperature. To anneal or refold RNA, oligonucleotides were dissolved in 50 mM potassium phosphate at pH 7.0, 50 mM KCl, 2 mM DTT, 2 mM

EDTA, heated to 95°C for 5 min and allowed to cool on ice for 1 h. All of these were further purified by FPLC using a Superdex 75 column (GE Healthcare) in a buffer containing 50 mM potassium phosphate at pH 7.0, 50 mM KCl, 2 mM DTT, 2 mM EDTA and concentrated. Single stranded nucleic acids were dissolved in 50 mM potassium phosphate at pH 7.0, 50 mM KCl, 2 mM DTT, 2 mM EDTA to get the final desired concentration. At the concentrations used for NMR titrations, the dsDNAs and dsRNAs are predicted to be at least 98% in duplex according to IDT.

### Preparation of histone tail peptides

Histone peptide corresponding to H3K14ac (9–19) was obtained from Bon Opus. All histone peptides were dissolved in $H_2O$ at a concentration of 20 mM determined by manufacturer determined weight, and the pH adjusted to ∼7.0.

### NMR spectroscopy and data analysis

NMR experiments were carried out on either an 800 MHz Bruker Avance II, Bruker Avance Neo 600 MHz, Bruker Avance II 500 MHz, Varian INOVA 600 MHz, or Varian 900 MHz all equipped with cryoprobes. To obtain backbone assignments for BD2 and BD4 (Supplementary Figures S13 and S14), HNCACB, CBCA(CO)NH, HNCO, and HN(CO)CA (53) (BD2 only) spectra were collected on $^{15}N,^{13}C$-labelled sample at 1mM on a Bruker 500 MHz (for BD4) and Bruker Avance Neo 600 MHz (for BD2) at 25°C. NMR data were processed using NMRPipe (54) and analyzed in CcpNmr (55). For the experiments carried out using nonuniform sampling, spectra were reconstituted with SMILES (56).

Titrations of wild-type and mutant BDs with oligonucleotides or acetylated peptides were carried out by collecting $^{1}H,^{15}N$ heteronuclear single quantum coherence (HSQC) spectra on $^{15}N$-labelled BDs at 0.1 mM in 93% $H_2O$/7% $D_2O$ at 25°C upon addition of increasing concentrations of substrate. NMR data were processed in NMRPipe (54) and analyzed in CcpNmr (55). The normalized chemical shift difference (Δδ) at every titration point was calculated as

$$\Delta\delta = \sqrt{(\Delta\delta_H)^2 + (0.154\Delta\delta_N)^2}$$

where $\Delta\delta_H$ and $\Delta\delta_N$ are the change in the $^{1}H$ and $^{15}N$ chemical shifts respectively between the apo state and each titration point. Dissociation constants ($K_d$s) were calculated by fitting the data to a single-site binding model accounting for ligand depletion in GraphPad Prism using the equation (57)

$$\Delta\delta = \Delta\delta_{max}\left(\frac{([L]+[P]+K_d) - \sqrt{([L]+[P]+K_d)^2 - 4[P][L]}}{2[P]}\right)$$

where [L] is the concentration of ligand, [P] is the concentration of the bromodomain and $\Delta\delta_{max}$ is the chemical shift change at saturation. Reported $K_d$ values were calculated as an average of individual values for residues with significant Δδ for each individual titration. Residues were determined to be significantly perturbed, if Δδ was greater than average Δδ plus 2 standard deviations of all residues (excluding unassigned residues) after trimming the 10% of residues with the largest Δδ.

### Cell culture conditions

Caki2 cells (American Type Culture Collection, Manassas, VA) were grown in McCoy's 5A medium (Corning Mediatech, Inc., Manassas, VA) supplemented with 10% fetal bovine serum (Corning Mediatech, Inc., Woodland, CA), 100 units/ml penicillin and 100 μg/ml streptomycin (Corning Mediatech, Inc.), 1% MEM nonessential amino acids (Corning Mediatech, Inc.), and 2 mM L-alanyl-L-glutamine (Corning Glutagro; Corning Mediatech, Inc.) at 37°C in a humidified atmosphere in a 5% $CO_2$ incubator.

### Generation of cell lines expressing full length PBRM1 mutants

A section of full length *PBRM1* (nucleotides 434–2130) with triple mutations (S275A,K277A,Y281A-SKY, K511A,R512A,K513A-KRK) were purchased from Biomatik and cloned into BstBI-digested PBRM1-TetO-FUW using the ligation-free In-Fusion HD cloning kit (Takara). The construct was packaged into lentivirus using HEK293T cells and delivered into target cells together with pLenti CMV rtTA3 Hygro (w785-1) (a gift from Eric Campeau Addgene plasmid no. 26730) for tetracycline inducible expression. The cells were selected with puromycin (2 μg/ml) and hygromycin B (200 μg/ml). To induce PBRM1 expression, Caki2 cells were treated with doxycycline (2 μg/ml) for at least 3 days.

### Nuclear lysates

Caki2 cells were tryspinized and washed in ice-cold phosphate buffered saline (PBS at pH 7.2). The pellet was resuspended in buffer A (20 mM HEPES at pH 7.9, 25 mM KCl, 10% glycerol, 0.1% Nonidet P-40 with protease inhibitors) at a concentration of 20 million cells/ml. The cells were kept on ice for 5 min, and nuclei were isolated by centrifugation at 600 × *g* (Eppendorf Centrifuge 5810 R, Hamburg, Germany) for 10 min. The nuclei pellet was resuspended in lysis buffer (50 mM Tris at pH 7.4, 150 mM NaCl, 1% Nonidet P-40, 1 mM EDTA, and protease inhibitors) at a concentration of 50 million nuclei/ml and rotated at 4°C for 30 min. The lysate was cleared by centrifugation at 20 000 × *g* for 10 min.

### Immunoblot analysis

Protein samples were mixed with 4x lithium dodecyl sulfate sample buffer containing 10% 2-merchaptoethanol. The protein lysates were denatured for 5 min at 95°C, separated on a 4–12% SDS-polyacrylamide gel, and transferred to a PVDF membrane (Immobilon FL, EMD Millipore, Billerica, MA). The membrane was blocked with 5% bovine serum albumin (VWR, Batavia, IL) in PBS containing 0.1% Tween-20 for one hour at room temperature and then incubated in primary antibodies overnight at 4°C. The pri-

mary antibodies were detected by incubating the membranes in goat anti-rabbit or goat anti-mouse secondary antibodies (LI-COR Biotechnology, Lincoln, NE) conjugated to IRDye 800CW or IRDye 680CW, respectively, for one hour at room temperature, and the signals were visualized using Odyssey Clx imager (LI-COR Biotechnology). Antibodies used for immunoblot: PBRM1 (Bethyl, A301-590A, 1:1000), ARID1A (Santa Cruz 1:1000) V5 (CST, D3H8Q, 1:1000), hnRNP A1 (Santa Cruz, 4B10 1:1000).

### Growth curve analysis

For growth curve analysis, 2000 (cell number) control or single/ triple mutant cells were plated in 96-well plates. After 7 days, the culture medium was aspirated and percent viability was assessed using CellTiter-Glo® reagent (Promega, Madison, WI). The luminescence was measured using Promega™ Glomax® luminometer.

### Cell proliferation competition assay

Caki2 parental cells were first transduced with lentiviral particles for the dual reporter construct pFU-Luc2-eGFP (L2G) (58) (a kind gift from Huiping Lui) and the GFP expressing cells were selected using FACS. These GFP positive cells were transduced with lentiviral particles for pLenti CMV rtTA3 Hygro (w785-1) (a gift from Eric Campeau Addgene plasmid number 26730) for tetracycline inducible expression and selected using hygromycin (200μg/ml). Once selected, these cells were transduced with lentiviral particles for TetO-Fuw empty vector (Addgene plasmid number 85747) (30). This cell line is referred to as Caki2 GFP-Fuw in the later sections.

Caki2 parental cells were transduced with rtTA and either TetO-Fuw empty vector, TetO-Fuw-PB1 WT (Addgene plasmid # 85746) (30), TetO-Fuw-PB1-SKY, or TetO-Fuw-PB1-KRK. All Caki2 cells were induced for protein expression using 2 μg/ml of doxycycline for 72 h, following which they were seeded in a 1:1 ratio in a 6-well plate and cultured in the presence of 2 μg/ml of doxycycline throughout the duration of the experiment. At 24 h post-seeding, each well was trypsinized and 1/4 of the harvested cells were re-seeded in a 6-well for the next timepoint while 3/4 of the harvested cells were analyzed by flow cytometry to determine GFP+ and GFP- populations. The 24 h GFP−/GFP+ ratio was used as a baseline for all the subsequent timepoints. The co-culture wells were harvested every 72–96 h depending on the confluency, such that the confluency never crossed 70%. Cell populations were analyzed using the Guava EasyCyte benchtop flow cytometer using monoculture cells as the controls and data analysis was done using FlowJo and GraphPad Prism.

### Serial salt extraction assay

Serial salt extraction assay was performed as published with minor modifications (59). Briefly, 5 million Caki2 cells were harvested by trypsinization and washed once with ice-cold PBS. The cells were lysed in modified buffer A (60 mM Tris, 60 mM KCl, 1 mM EDTA, 0.3 M sucrose, 0.5% Nonidet P-40, 1 mM DTT) with protease inhibitor and deacetylases inhibitor, and nuclei were pelleted. The nuclei were then incubated in 200 μl of extraction buffer 0 (50 mM HEPES at pH 7.8, 2% NP-40, 0.5% sodium deoxycholate, 1 mM DTT, protease inhibitors and deacetylase inhibitor) for 10 min and centrifuged at 7000 × *g* for 5 min, and the supernatant was collected as '0 mM fraction'. The pellet was then resuspended in 200 μl of extraction buffer 100 (50 mM HEPES at pH 7.8, 2% NP-40, 0.5% sodium deoxycholate,1 mM DTT, protease inhibitors, 100 mM NaCl) and processed in the same manner to yield '100 mM fraction.' Serial extraction was implemented with extraction buffers containing 200, 300, 400 and 500 mM NaCl. Aliquots from each fraction (20 μl) were mixed with 4× lithium dodecyl sulfate loading buffer for immunoblotting.

### ChIP-seq

Caki2 cells were treated for 6 days in 15cm plates with doxycycline (2 μg/ml) and were ∼80–90% confluent on the day of harvesting (∼8–10 million cells/15 cm at harvest). Cells were either cross-linked with 1% formaldehyde only (H3K14ac ChIP-seq) for 10 min at 25°C or dual crosslinked (PHF10 ChIP-seq) with 2mM DSG for 45 min at 25°C followed by 1% formaldehyde for 10 min at 25°C as described in (60). Crosslinking was quenched with 125 mM Glycine, for 10 min at 25°C. The cells were washed with ice-cold 1× PBS, scraped into 15 ml tubes, pelleted, flash frozen with liquid nitrogen, and stored at −80°C until ready for processing. Cell pellets were thawed on ice, extracted with nuclear extraction buffer (50 mM HEPES–KOH pH 8.0, 140 mM NaCl, 1 mM EDTA, 10% glycerol, 0.5% NP-40, 0.25% Triton X-100) for 10 min on ice and washed once with nuclear wash buffer (10 mM Tris–HCl pH 8.0, 1mM EDTA, 0.5mM EGTA, 200 mM NaCl). Nuclear pellets were resuspended in shearing buffer (10 mM Tris–HCl pH 8.0, 1mM EDTA, 0.1% SDS) and sonicated using Branson SFX250 at 10% amplitude for 9–10 min at 0.5s ON and 1.5 s OFF setting to obtain 200–800 bp fragment size. Sonicated chromatin was clarified by high-speed centrifugation and a 50 μl aliquot was reverse cross-linked to check shearing efficiency. The chromatin was quantitated using absorbance at 260 nm and further diluted with 5× ChIP dilution buffer (250 mM HEPES–KOH pH 7.5, 1.5 M NaCl, 5mM EDTA, 5% Triton X-100, 0.5% sodium deoxycholate, 0.5% SDS) to obtain equal chromatin amounts in equal volume. For H3K14ac ChIP-seq, 2 μl of EpiCypher K-AcylStat panel designer nucleosomes were added as spike-in to all samples, 2.5% of the sample was taken out as input and anti-H3K14ac (1:200, 07-353 Millipore Sigma) was added. For PHF10 ChIP-seq, 5% mouse chromatin (NMuMG cells) was added as spike-in, 2.5% of the sample was taken out as input, and anti-PHF10 (1:100, PA5-30678 Invitrogen) was added. After overnight primary antibody incubation at 4°C with rotation, Protein A Dynabeads (7.5 μl per μg of antibody) were added and rotated at 4°C for another 2h. The beads were sequentially washed with low-salt wash buffer (20 mM HEPES–KOH pH 7.5, 0.1% SDS, 0.1% deoxycholate, 1% Triton, 150 mM NaCl, 1 mM EDTA, 0.5 mM EGTA), high-salt wash buffer (20 mM HEPES–KOH pH 7.5, 0.1% SDS, 0.1% deoxycholate, 1% Triton, 500 mM NaCl, 1 mM EDTA, 0.5mM EGTA), LiCl wash buffer (20 mM HEPES–

KOH pH 7.5; 0.5% deoxycholate, 0.5% IGEPAL CA-630; 250 mM LiCl, 1 mM EDTA, 0.5 mM EGTA) and final wash buffer (20 mM HEPES–KOH pH 7.5, 1 mM EDTA, 0.5 mM EGTA). The immunoprecipitated chromatin was eluted once with 200 μl and once with 100 μl elution buffer (100 mM $NaHCO_3$, 1% SDS) for 30 min each at 37°C with shaking. The eluate and the saved input were treated with 2 μl RNase A (10 mg/ml, Thermo Scientific EN0531), 2 ul Proteinase K (20 mg/ml, Thermo Scientific EO0491) and reverse cross-linked at 65°C for 16 h. DNA was extracted once with phenol:chloroform; once with chloroform and precipitated by adding 1/10 volume of 3 M NaOAc pH 5.2; 1 volume 2-propanol and 2 μl glycogen (20 mg/ml, Thermo Scientific R0561) overnight at −20°C. After centrifugation at top speed for 1 h, the pellet was washed with fresh 70% ethanol and then air-dried. DNA was resuspended in low-EDTA TE buffer and DNA quality, and concentration were determined using Qubit and Agilent TapeStation (Purdue Genomics Core Facility). ChIP-seq library preparation was done using Ovation Ultralow System V2 UDI according to manufacturer's directions and the final library was subjected to double sided size selection of 0.65× and 1× with Ampure beads. Library DNA quality and concentration were determined using Qubit and Agilent TapeStation (Purdue Genomics Core Facility). Equimolar library pools were generated using cluster numbers obtained from MiSeq and submitted for 150 bp PE sequencing on NovaSeq 6000 platform (Novogene, Sacramento, CA).

### ChIP-seq analysis

ChIP-seq data analysis was performed using *Partek® Flow®* software, v10.0. Raw sequencing reads were trimmed for adapter content and quality (Quality cut-off >20) and aligned to hg38 using Bowtie2 allowing 1 seed mismatch (broad regions = yes for PHF10 ChIP-seq). MACS was used for peak calling.

### Spike-in normalization strategy

For PHF10 ChIP-seq, reads that did not align to hg38 were aligned to mm10 using Bowtie2 allowing 1 seed mismatch (Broad regions = yes for PHF10 ChIP-seq). The IP efficiency was determined by calculating the percent of reads for 30 high confidence PHF10 peaks from mouse cells (unpublished data) using DeepTools plotenrichment in Galaxy. The relative enrichment was calculated based on the lowest enrichment sample and the remaining samples were downsampled using Picard Tools in Galaxy. For H3K14ac ChIP-seq, designer Nucs (dNucs) from EpiCypher were added to each sample before setting up IP. These dNucs are a barcoded pool of 22 different histone lysine-acetylation marks and an unmodified nucleosome to enable antibody specificity calculations for histone PTM ChIP. Each nucleosome has 2 barcodes: one common to all in that panel (K-AcylStat panel) and one specific to each acetylation mark within the panel. The number of reads corresponding to each barcode was calculated for each input and IP by Basepair Tech©.

### Cross linking immunoprecipitation (CLIP)

Caki2 cells were washed in ice-cold phosphate buffered saline (PBS at pH 7.2) and irradiated in PBS at 200 mJ/cm$^2$ using SpectroLinker XL_1000 UV crosslinker. The pellet was resuspended in buffer A (20 mM HEPES at pH 7.9, 25 mM KCl, 10% glycerol, 0.1% Nonidet P-40 with PMSF, aprotinin, leupeptin, and pepstatin, DTT, SAHA) at a concentration of 20 million cells/ml. The cells were kept on ice for 5 min, and nuclei were isolated by centrifugation at 600 × *g* (Eppendorf Centrifuge 5810 R, Hamburg, Germany) for 10 min. The nuclei pellet was resuspended in RIPA buffer (50 mM Tris at pH 7.4, 150 mM NaCl, 1% Nonidet P-40, 0.1% SDS, 0.5% sodium deoxycholate supplemented with PMSF, aprotinin, leupeptin, and pepstatin, DTT, SAHA) and incubated on ice for 5 min. 1:50 dilution of RNase cocktail (Ambion, Inc., Foster City, CA; 500 U/ml RNase A + 20 000 U/ml RNase T1) and 4U of Turbo DNase (Invitrogen, 2 U/μl) were added to extracts and incubated at 37°C for 3 min. The extracts were cleared by centrifugation (Centrifuge 5424 R; Eppendorf, Hamburg, Germany) at 21 000 × *g* for 30 min. One microgram specific antibody was used per 200 μl lysate for immunoprecipitation V5 (CST, D3H8Q, 1:200 IP), or hnRNP A1 (Santa Cruz, 4B10 1:200 IP). After 1 hour incubation, immunocomplexes were captured using protein A magnetic beads following a 2 h incubation. The beads were washed twice in high salt buffer (50 mM Tris at pH 7.9, 1 M NaCl, 1 mM EDTA, 1M Urea, 1% Nonidet P-40, 0.1% SDS, 0.5% sodium deoxycholate, with PMSF, aprotinin, leupeptin, and pepstatin, DTT, SAHA, ribo-out) followed by two washes in low salt buffer (20 mM Tris at pH 7.9, 0.2% Tween-20, 10 mM $MgCl_2$ with PMSF, aprotinin, leupeptin, and pepstatin, DTT, SAHA, ribo-out). The beads were resuspended in 500 μl of low salt buffer and divided 1:3 for western blot and PNK labeling. The western blot protein samples were eluted in 1× lithium dodecyl sulfate loading dye (Thermo Scientific) by boiling at 95°C for 5 min. For PNK labeling, PNK enzyme (Thermo Scientific, VA) and $\gamma$-$^{32}$P-ATP (PerkinElmer) were added to the beads and incubated at 37°C for 30 min. The hot reaction mix was removed, the beads were boiled in 1× loading dye, the proteins were separated on a 4–12% SDS-polyacrylamide gel and labeled proteins were imaged using a phosphorimager (Typhoon® FLA9500).

### CLIP-seq

The CLIP-seq was performed using the eCLIP-RBP kit from Eclipse BioInnovations© according to the manufacturer's instructions with the following specifications. Caki2 cells (15 million) from each cell line were trypsinized and resuspended in 1 ml PBS in a 6 cm dish placed on ice. The cells were crosslinked at 400 mJ/cm$^2$ in a SpectroLinker XL_1000 UV crosslinker, pelleted, flash frozen, and stored at −80°C until lysis. Additional steps were followed according to the manufacturer's instructions and 150 μg RNA and 2 μl V5 antibody (Cell Signaling Technology, #13202) was used for each IP. Instead of gel purification, 20% of the cDNA was amplified and the final library was subjected to double sided size selection of 0.5× and 0.9× with Ampure

beads. Library DNA quality and concentration were determined using Qubit and Agilent TapeStation (Purdue Genomics Core Facility). Equimolar library pools were generated using cluster numbers obtained from MiSeq and submitted for 150 bp PE sequencing on NovaSeq 6000 platform (Novogene, Sacramento, CA). SE reads were used for analysis by Eclipsebio using the following pipeline 'The RBP-eCLIP data processing pipeline begins with UMI (unique molecular identifiers) trimming and adapter trimming of raw sequencing reads, then reads are filtered of repetitive genome elements such as rRNA and aligned to the reference genome (i.e. human.). Once aligned, PCR duplicates are removed, and clusters of reads are identified to define peaks in the data representing RBP binding sites. Finally, peaks and genes containing peaks are analyzed in detail to reveal binding features for the RBP of interest. Additional analysis of peaks was performed using BAM files in Galaxy using MACS, BedTools, and DeepTools. For integrating CLIP-seq and ChIP-seq data with Caki2 RNA-seq data, raw sequencing reads were downloaded for GSE76199 (61) from GEO and analyzed using Partek® Flow® software, v10.0. Raw sequencing reads were trimmed for adapter content and quality (Quality cutoff >20) and aligned to hg38 using STAR aligner. The aligned BAM files were converted to BigWig files using DeepTools bamCoverage with–normalizeUsing RPKM option.

## RESULTS

### PBRM1 BD2 and BD4 selectively associate with RNA

To initially test the nucleic acid binding activity of PBRM1 BDs, electromobility shift assays (EMSAs) were performed for each BD individually with the 147 base-pair (bp) Widom 601 DNA. Consistent with our previous hypothesis (46), the addition of increasing concentrations of BD2, BD3, BD4 and BD5 resulted in a shift in the migration of DNA, indicative of binding (Supplementary Figure S2). In contrast, no shift was observed for BD1 and BD6 at any of the concentrations tested, consistent with no to very weak DNA binding of these BDs (Supplementary Figure S2).

To further characterize these interactions, we utilized nuclear magnetic resonance (NMR) spectroscopy. Initial $^{1}H$,$^{15}N$ heteronuclear single quantum coherence ($^{1}H$,$^{15}N$-HSQC) spectra of each BD revealed well-dispersed resonances in both $^{1}H$ and $^{15}N$ dimensions, indicating that all domains are well-folded (Supplementary Figure S3). However, BD3 and BD5 were unstable over time (data not shown), and as such, we focused all further studies on BD2 and BD4.

To assess the nucleic acid selectivity of BD2 and BD4, we tested binding to four nucleic acid substrates: 11 bp double-stranded DNA (dsDNA), 13 nucleotide (nt) single-stranded DNA (ssDNA), 30nt stem-loop RNA (dsRNAI), and 13nt poly-U ssRNA (ssRNAI) (see Figure 1B). The chosen DNA sequence in the double stranded substrate has been found to bind the BRG1/BRM BDs previously (62), dsRNAI is nearly identical in sequence to the DNA but with an added UUCG loop and GC-pair to favor formation of the stem-loop, and the poly-U was chosen to ensure single-stranded nature. $^{1}H$-$^{15}N$ HSQC spectra were collected on $^{15}N$-labeled BD2 or BD4 upon titration of each oligonucleotide substrate (Figure 1C, Supplementary Figures S4 and S5). Chemical shift perturbations (CSPs) were observed in BD2 and BD4 resonances upon increasing concentrations of all substrates tested, consistent with binding. Dissociation constants were calculated by plotting the normalized CSPs as a function of substrate concentration and fitting to a single-site binding model accounting for ligand depletion (see methods). This revealed that BD2 has the highest affinity for the stem-loop dsRNAI ($K_d = 0.025 \pm 0.008$ mM, Figure 1D) compared to substantially weaker affinity for dsDNA ($K_d = 0.91 \pm 0.38$ mM), ssRNAI ($K_d = 0.35 \pm 0.08$ mM) and ssDNA ($K_d = 0.13 \pm 0.03$ mM). BD4 also demonstrated the highest affinity for the stem-loop dsRNAI, albeit with weaker overall affinity as compared to BD2 ($K_d = 0.12 \pm 0.02$ mM, Figure 1E). In comparison, dsDNA bound with $K_d = 0.50 \pm 0.27$ mM, and ssDNA and ssRNAI bound with $K_d = 2.97 \pm 0.14$ mM and $K_d = 0.32 \pm 0.14$ mM, respectively. The relative affinity of each BD for the individual substrates supports that each has selectivity for stem-loop RNA amongst the substrates tested here.

To better understand the selectivity for the stem-loop RNA, we investigated additional RNA substrates, including two additional stem-loop structures and a dsRNA lacking any loop (Figure 2C). CSPs were observed in both BD2 and BD4 upon titration of all dsRNA substrates (Figure 2A, B, Supplementary Figures S4 and S5). Notably, for the majority of residues, the CSPs follow the same trajectory for all stem-loops, as well as the dsRNA lacking a loop. The exception is M282 of BD2, which has slightly different trajectories for dsDNA, stem-loop RNAs, and dsRNA lacking the loop. In addition, the calculated $K_d$ values were similar for all dsRNA substrates for both BDs, but overall weaker for BD4 as compared to BD2 (Figure 2D). Together, this suggests that the association of BD2 and BD4 with RNA is not dependent on the loop, and rather that both BDs are selectively interacting with double-stranded RNA elements.

### BD2 and BD4 bind RNA through distinct binding pockets

RNA binding pockets on BD2 and BD4 were identified by plotting the normalized CSPs as a function of BD residue. For BD2, association with dsRNAI leads to the largest CSPs in residues in the BC loop and αC helix with smaller perturbations observed in the αB helix and ZA loop (Figure 3A). Notably, all three stem-loop RNAs and the dsRNA with no loop demonstrated nearly identical binding pockets on BD2, suggesting an identical mechanism of binding to these substrates and consistent with the loop playing no role in the interaction (Supplementary Figure S6). Mapping the CSPs onto a previously solved structure of BD2 reveals that these residues cluster along one face of the alpha-helical bundle formed by αB and αC, that coincides with a highly basic surface patch (Figure 3C and Supplementary Figure S7a).

A similar analysis for BD4 reveals a distinct binding pocket with the most perturbed residues in a region N-terminal to the αZ helix as well as in αZ, and similarly in the residues C-terminal to the αC helix and in αC. Smaller perturbations are also observed in the αB helix and ZA loop (Figure 3B). Mapping these onto a previously solved crys-

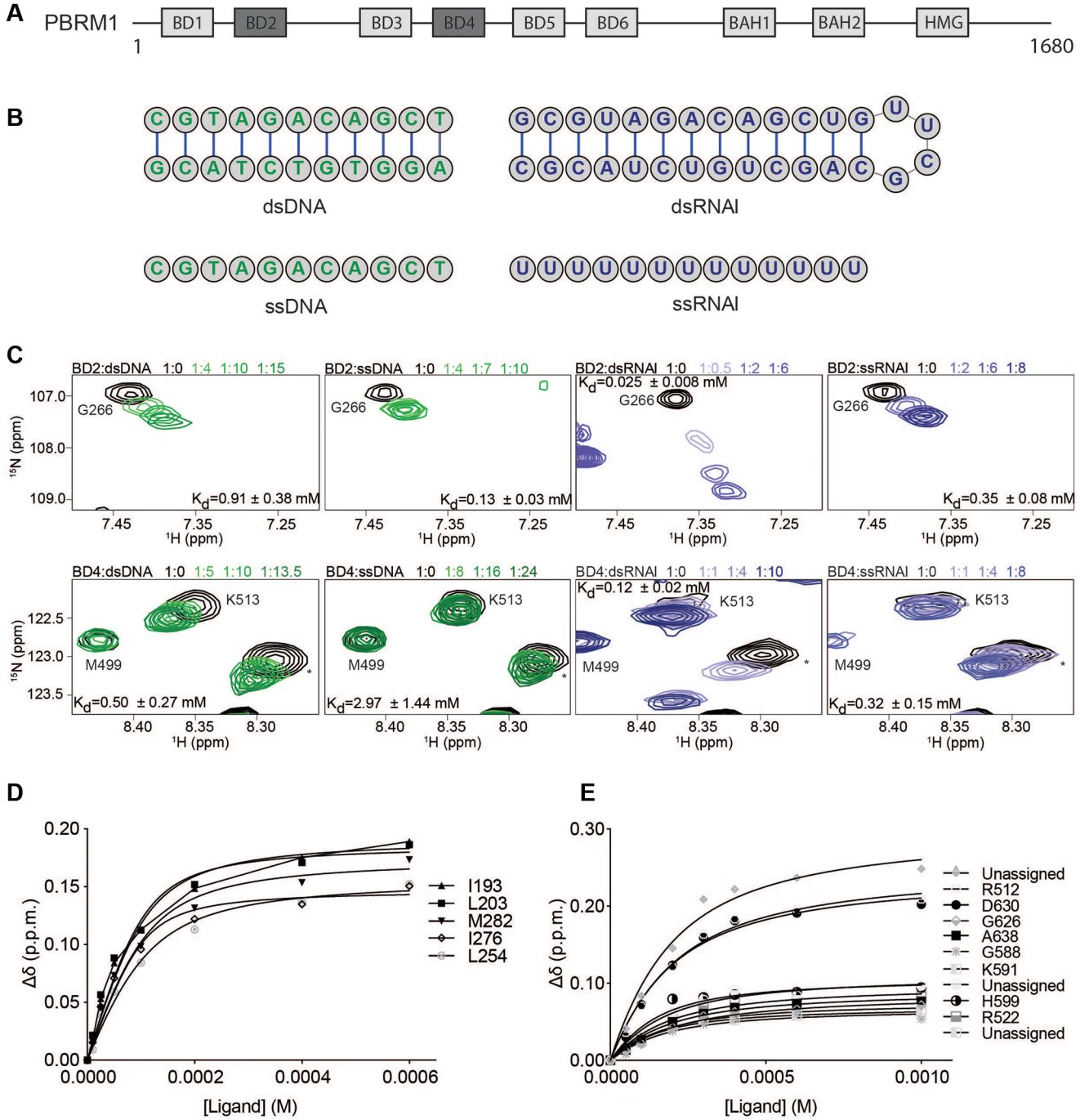


**Figure 1.** PBRM1 BD2 and BD4 selectively bind to RNA. (**A**) The domain architecture of the PBRM1 subunit of the PBAF complex. BD2 and BD4 are colored dark grey. (**B**) Structures of double stranded (top) and single stranded (bottom) DNA (green) and RNA (purple) used for NMR titrations shown in (C). (**C**) Overlay of $^{1}H$–$^{15}N$ HSQC spectra of $^{15}N$-BD2 (top row) or $^{15}N$-BD4 (bottom row) upon titration with dsDNA, ssDNA, dsRNAI or ssRNAI. The spectra are color coded according to protein:nucleic acid molar ratio as shown in the legend. For clarity, only 4 titration points are displayed. For BD2 dsDNA titration was collected at 1:0, 1:1, 1:2, 1:4, 1:6, 1:10, 1:12, 1:15, ssDNA was collected at 1:0, 1:0.5, 1:1, 1:2, 1:4, 1:7, 1:10, dsRNAI was collected at 1:0, 1:0.1, 1:0.25, 1:0.5, 1:1, 1:2, 1:4, 1:6 and ssRNAI was collected at 1:0, 1:1, 1:2, 1:4, 1:6, 1:8. For BD4 sDNA titration was collected at 1:0, 1:0.5, 1:1, 1:2, 1:2.5, 1:5, 1:7.5, 1:10, 1:13.5, ssDNA was collected at 1:0, 1:0.5, 1:1, 1:4, 1:8, 1:12, 1:16, 1:24, dsRNAI was collected at 1:0, 1:0.5, 1:1, 1:2, 1:3, 1:4, 1:6, 1:10 and ssRNAI was collected at 1:0, 1:1, 1:2, 1:4, 1:6, 1:8. (**D, E**) Binding curves calculated from the normalized chemical shifts for BD2 (D) or BD4 (E) upon binding to dsRNAI. Titration points are fit to a single-site binding model under ligand-depleted conditions.

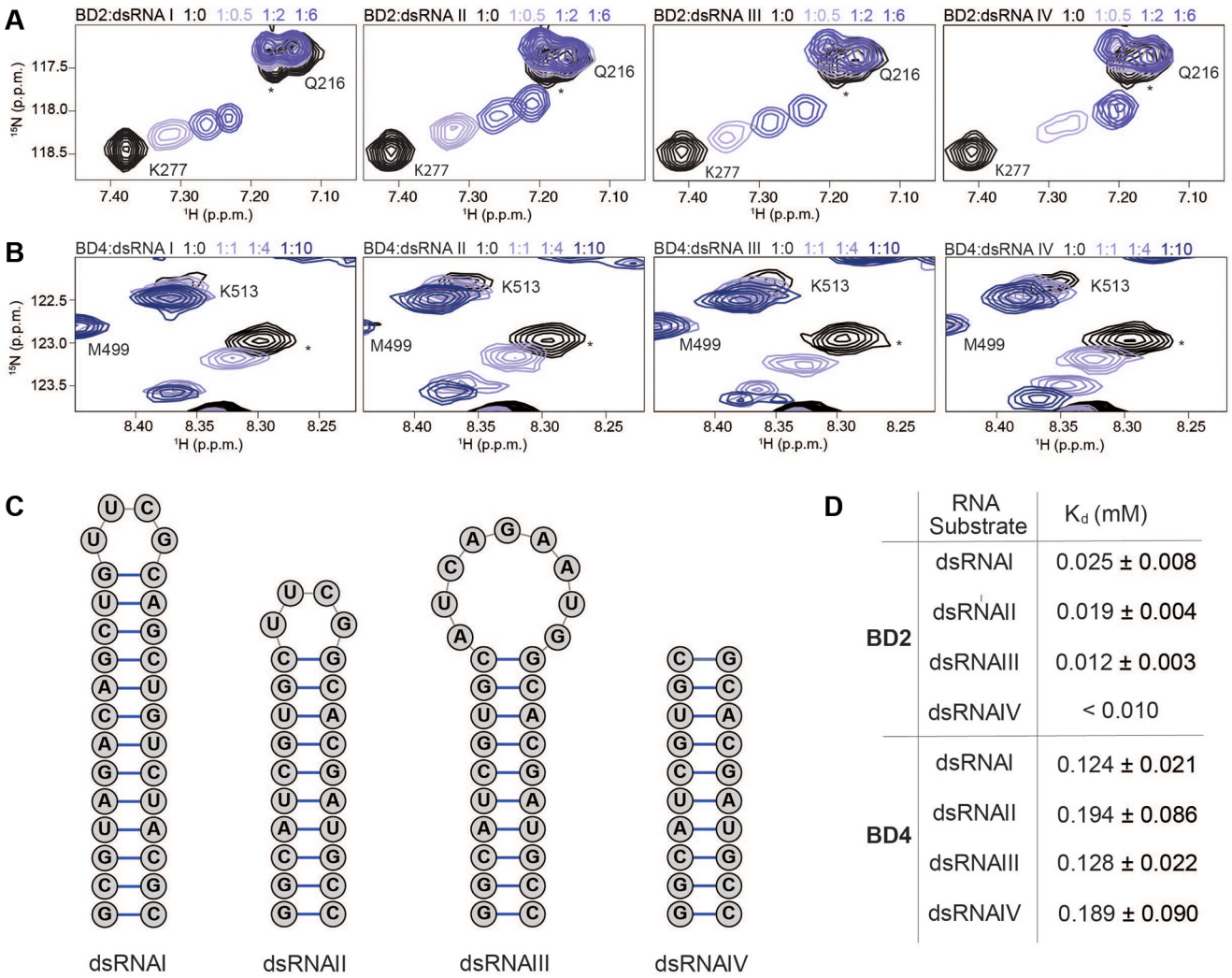


**Figure 2.** BD2 and BD4 preferentially associate with double stranded RNA elements. (**A, B**) Overlay of $^{1}H$–$^{15}N$ HSQC spectra of $^{15}N$-BD2 (A) or $^{15}N$-BD4 (B) upon titration with different dsRNA substrates (see C). The spectra are color coded according to protein:RNA molar ratio as shown in the legend. For clarity, only 4 points are displayed. For BD2, all dsRNA titrations were collected at 1:0, 1:0.1, 1:0.25, 1:0.5, 1:1, 1:2, 1:4, 1:6. For BD4, all titrations were collected at 1:0, 1:0.5, 1:1, 1:2, 1:3, 1:4, 1:6, 1:10. (**C**) Schematics of dsRNA substrates used for NMR titrations in the study. (**D**) Dissociation constants ($K_d$) determined from NMR titrations with $^{15}N$-PBRM1 BD2 and BD4 with double stranded RNA substrates. $K_d$ values are fit to a single-site binding model under ligand-depleted conditions using 7–9 titration points. Shown are the averages over individual residues with significant CSPs and associated standard deviation. For dsRNAIV association with BD2 the calculated $K_d$ was less than 1/10 the protein concentration and thus stated as the upper limit.

tal structure of BD4 reveals a much more extended binding pocket as compared to BD2, spanning from the bottom of the alpha-helical bundle to the ZA loop, but also coinciding with an elongated basic patch (Figure 3C and Supplementary Figure S7b). The residues at the N- and C-termini were not included in the construct used for the crystal structure. However, analysis of the HN, N, Cα, Cβ, and CO chemical shifts using TALOS+ (63) (Supplementary Figure S7c) or a calculated SSP score (64) (Supplementary Figure S7d) indicate that these residues are largely disordered though with some helical propensity in both N and C termini. As observed for BD2, all three stem-loops and the dsRNA without a loop interact with nearly identical binding pockets on BD4 (Supplementary Figure S8).

For BD2, ssRNA, ssDNA and dsDNA substrates led to CSPs in nearly identical residues as compared to dsRNA but led to substantially lower magnitudes of CSPs consistent with a less stable complex (Supplementary Figures S6 and S8). A similar effect is seen for BD4 with ssRNA and dsDNA. Notably, BD4 has some additional residues that are perturbed upon addition of ssDNA but overall the magnitude of CSPs are still quite small as compared to RNA (Supplementary Figure S8).

### RNA association enhances histone tail binding

Both BD2 and BD4 have previously been shown to preferentially associate with H3K14ac peptides and are the most critical BDs for PBRM1 association with H3K14ac nucleosomes (43). To investigate how histone and RNA binding integrate, we utilized NMR spectroscopy. Specifically binding of $^{15}N$-labeled BD2 or BD4 to an H3K14ac peptide was assessed in the absence of, or when pre-bound to dsRNAI.

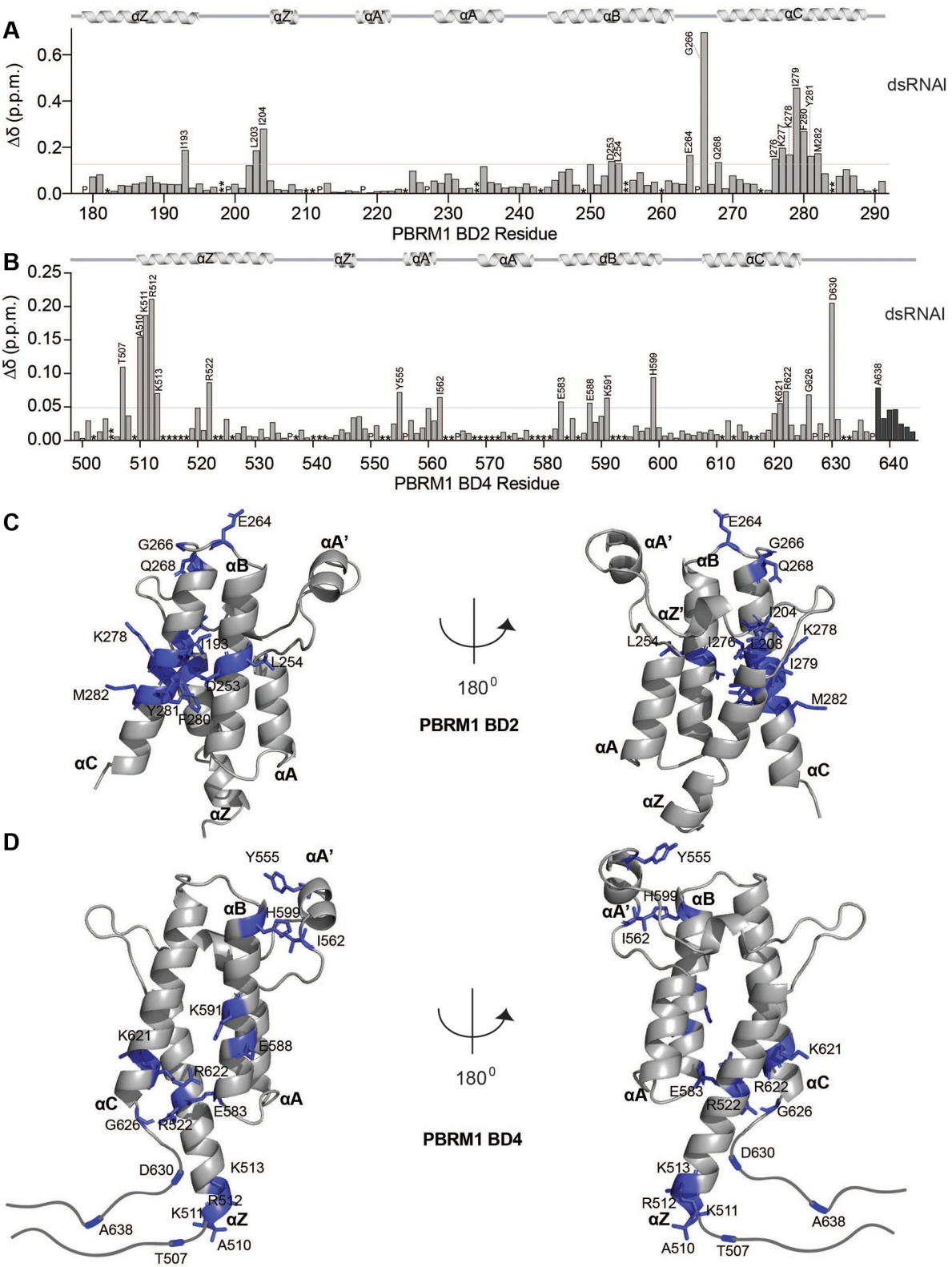


**Figure 3.** BD2 and BD4 bind RNA through distinct binding pockets. (**A, B**) Normalized chemical shift changes between apo and RNA-bound (Δδ) plotted as a function of residue for BD2 (A, 1:6 of BD2:dsRNAI) or BD4 (B, 1:10 of BD4:dsRNAI). Prolines are marked as (P), residues that are unassigned in the apo are marked as (*), residues for which the bound states were not trackable due to overlap are marked as (**), residues that broadened beyond detection are marked as (***). The secondary structure of the BDs is denoted above the plots, and residues that were perturbed greater than the average plus two standard deviations (grey line) after trimming off the top 10% are labelled. (**C, D**) Residues significantly perturbed upon addition of dsRNAI are shown as purple sticks and labeled on the previously solved structure of BD2 (C, PDB ID 3HMF) or BD4 (D, PDB ID 3TLP) with the secondary structure elements labelled.

As expected, addition of H3K14ac peptide led to significant CSPs in BD2 and BD4 (Figure 4A, B, top panels; Supplementary Figure S9a, Supplementary Figure S10a). Consistent with previous studies, perturbations were most significant for residues in the ZA loop, BC loop, and residues just in the top of the αB and αC helices (Figure 4A, B, top panels). Comparison of CSPs induced by H3K14ac with those induced by dsRNAI (Figure 4A, B, top and middle panels) revealed that the histone and RNA binding pockets are partially overlapping for both BD2 and BD4. Residues in BD2 that are significantly perturbed by the addition of both dsRNAI and H3K14ac include E264, G266 and Q268 in the BC loop. For BD4 residues in the ZA loop are perturbed by both dsRNAI and H3K14ac (Supplementary Figure S11).

To test if the BDs can bind to both histone tail and RNA simultaneously, H3K14ac peptide was titrated into dsRNAI-bound BD. For residues that are perturbed by peptide but not RNA, addition of peptide in the presence of RNA led to CSPs that are nearly identical to those seen without RNA present (Figure 4A, B, bottom panels; Supplementary Figures S9b and S10b). For residues that are perturbed by RNA but not peptide, addition of peptide in the presence of RNA did not lead to any further perturbations. Together this supports that BD2 and BD4 can bind to both RNA and peptide simultaneously. Notably, a subset of residues adopted a unique bound-state chemical shift in the presence of both RNA and peptide indicating a unique conformation of these residues in the ternary complex (see Supplementary Figure S12). For BD2, this includes; I204 in the ZA loop; I228, Q235 in the αA helix; Y261, N263, E264, S267, V269 in the BC loop; and K270, K271, I276, K277, K278, I279, F280 and M282 in the αC helix. For BD4 this includes; Y555, I562 in the ZA loop; E583 and Y599 in the αB helix; and K621 in the αC helix.

To assess the effect of RNA association on histone binding, affinities for the peptide were determined from the CSPs and compared in the absence and presence of RNA. For BD2 the $K_d$ decreased from 0.41 ± 0.03 mM for H3K14ac alone to 0.32 ± 0.06 mM when pre-bound to dsRNAI ($P$-value < 0.0001), indicating increased affinity. Similarly, for BD4 the $K_d$ for H3K14ac peptide decreased from 0.57 ± 0.06 mM to 0.30 ± 0.03 mM in the presence of RNA. Notably, this increase in affinity was not observed for BD4 when pre-bound to DNA ($K_d$ = 0.63 ± 0.18 mM), revealing that this is unique to dsRNA.

### BD2 and BD4 nucleic acid binding residues contribute to PBRM1-mediated cellular function

To assess the functional importance of RNA binding, we first identified BD2 and BD4 mutations that inhibit RNA binding. From the NMR titrations with dsRNAI, residues with substantial CSPs upon titration of RNA (and not histone) were mutated to alanine: S275, K277 and Y281 in BD2, and K511, R512 and K513 in BD4. NMR $^{1}H,^{15}N$-HSQC spectra confirmed that mutated BD2 and BD4 both retain their fold (Supplementary Figure S15) and still associate with H3K14ac peptides (Supplementary Figures S16 and S17). Titration of dsRNAI into BD2 S275A,K277A,Y281A mutant revealed $K_d$ = 0.20 mM ± 0.07 mM corresponding to a ∼8-fold reduction in affinity (Figure 5A, Supplementary Figure S15a). Similarly, titration of dsRNAI into BD4 K511A,R512A,K513A mutant revealed a $K_d$ of 1.02 ± 0.04 mM corresponding to a ∼8-fold reduction in affinity (Figure 5A; Supplementary Figure S15b).

To determine whether mutating the RNA-binding residues of BD2 and BD4 can affect PBRM1 function in cells, we utilized the PBRM1-null renal cancer cell line Caki2 (42,61). PBRM1 is a confirmed tumor suppressor when deleted with VHL in mouse models of renal cancer (65–67); however, PBRM1 deletion in most cells leads to either no change or context-dependent effects on growth rates (68–70). Similarly, in most PBRM1-deficient renal cancer cell lines, re-expression of PBRM1 has no effect on cell proliferation (61). In Caki2 cells, however, PBRM1 re-expression induces a consistent, although modest, decrease in cell growth, ranging between a 20–30% decrease in cell number compared to parental lines (61). In our previous publication, we mutated the conserved asparagine involved in acetyl-lysine binding in each of PBRM1's BDs. We found that mutation in the BD2, BD4 or BD5 abrogated the ability of full length PBRM1 to suppress the growth rate of Caki2 cells (71). Using a similar strategy here, the triple mutants in BD2 or BD4 (S275A,K277A,Y281A-SKY, and K511A,R512A,K513A-KRK) were incorporated into full length PBRM1 and re-expressed in Caki2 cells (Figure 5B). Re-expression of WT PBRM1 into Caki2 cells significantly slows growth compared to control (30), and this growth suppression is significantly reduced in the PBRM1 BD2 (SKY) and BD4 (KRK) mutant cells (Figure 5C, Supplementary Figure S18a). Due to variability in Caki2 growth rates from differences in cell density or cell culture conditions that can propagate through multiple cell divisions, we developed a second FACS-based competition assay using co-culture with GFP-labeled Caki2 cells as an internal control. Using this assay, we found Caki2 GFP-labeled cells can outcompete Caki2 cells expressing WT PBRM1, but not Caki2 cells with vector alone (Figure 5D, Supplementary Figure S18b). Caki2 cells expressing PBRM1 with triple mutations in BD2 (SKY) and BD4 (KRK) display a greater ability to outcompete Caki2 GFP-labeled cells than Caki2 cells expressing WT PBRM1 (Figure 5D), which was consistent over multiple experiments (Supplementary Figure S18c). This indicates that mutation in nucleic acid binding residues of BD2 and BD4 affects the growth suppressive function of PBRM1 in renal cancer cells.

Since BD2 and BD4 can associate with both DNA and RNA substrates, we next determined how mutations in BD2 and BD4 affect the overall affinity of PBRM1 for bulk chromatin containing RNA, DNA, histones, and associated proteins. For this, we employed a sequential salt extraction (SSE) assay, which measures the relative affinity of nuclear proteins to bulk chromatin (59). PBRM1 is the last subunit to be incorporated in PBAF and is not necessary for the assembly of other subunits into a functional PBAF complex (61,72). Additionally, PBAF without PBRM1 can still associate with chromatin (71) and regulate a subset of PBAF transcriptional targets (73). In Caki2 cells without PBRM1 expression, we previously found that

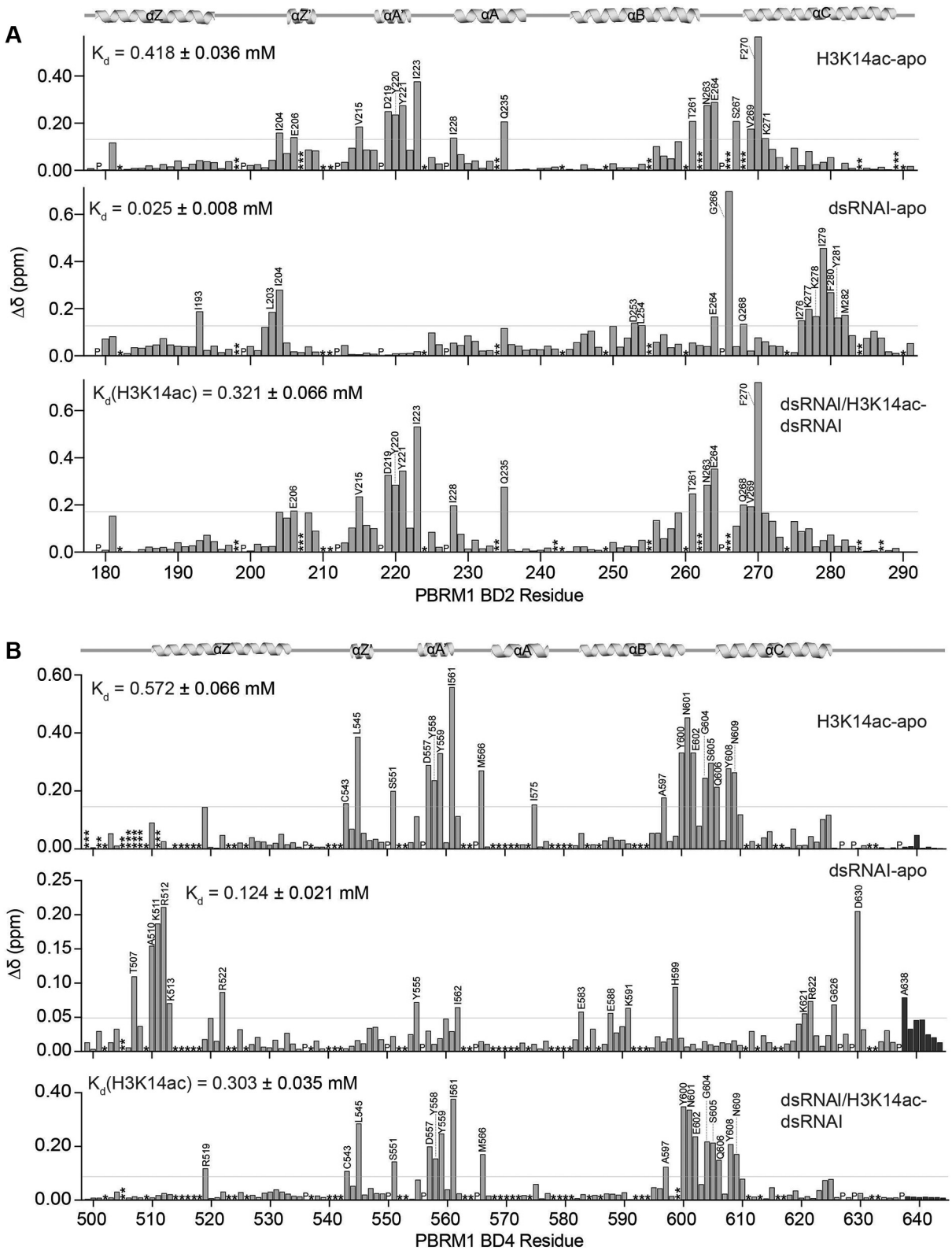


**Figure 4.** BD2 and BD4 have partially overlapping nucleic acid and histone binding pockets. (**A, B**) Normalized chemical shift changes (Δδ) between apo and H3K14ac-bound (top), apo and dsRNAI-bound (middle), and dsRNAI-bound and H3K14ac-bound (bottom) for BD2 (A) and BD4 (B). Protein:dsRNAI, protein:H3K14ac, protein:dsRNAI:H3K14ac are in molar ratio of 1:6, 1:10 and 1:6:10 respectively for BD2. Protein:dsRNAI, protein:H3K14ac, protein:dsRNAI:H3K14ac are in molar ratio of 1:10, 1:40 and 1:10:15 respectively for BD4. Residues that are unassigned, merged with the addition of ligand, or broaden beyond detection upon addition of ligand, are marked as (*), (**) and (***), respectively. The secondary structure of the BD2 is denoted above the plots, and residues that were perturbed greater than the average plus two standard deviations (grey line) after trimming off the top 10% of CSPs are labelled.

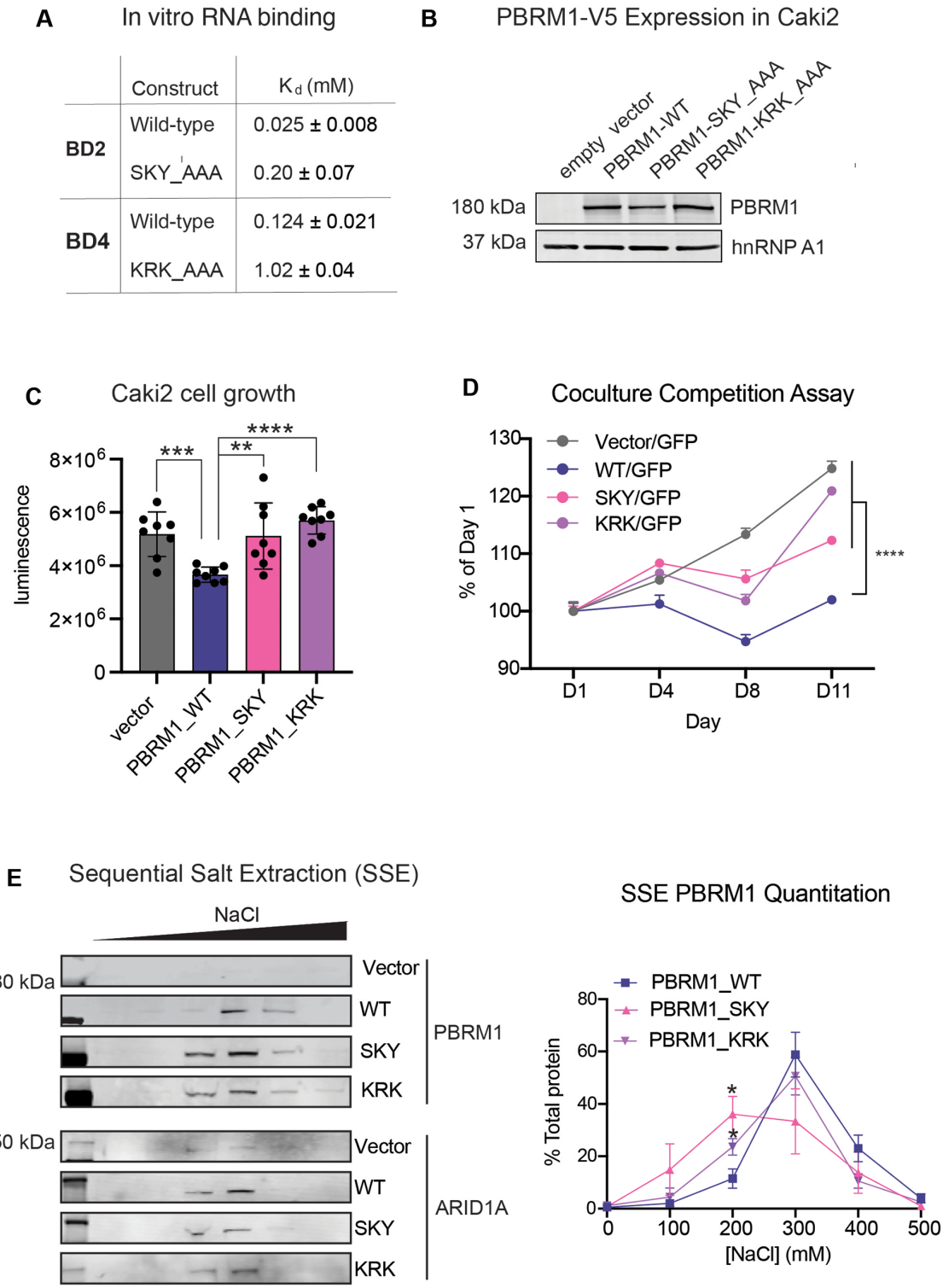


**Figure 5.** Mutation of RNA-binding residues disrupts PBRM1 function in cells. (**A**) Dissociation constants ($K_d$) determined by NMR for wild-type and mutant BD2 and BD4. (**B**) Immunoblot analysis of lysates from Caki2 renal clear cell carcinoma cells expressing full length WT PBRM1 or PBRM1 containing three amino acid mutations in BD2 or BD4. hnRNPA1 is included as a loading control. (**C**) CellTiter-Glo® measurement of viable cells for seven days of culture of 2000 cells plated in 96-well plates. A designation of * $P < 0.05$, ** $P < 0.01$, *** $P < 0.001$, **** $P < 0.0001$ (paired Student $t$-test). Error bars represent s.d. $n = 8$. (**D**) The change in the proportion of GFP negative cells compared to GFP positive cells as measured by flow cytometry. Equal numbers of GFP-labeled Caki2 cells and Caki2 cells expressing inducible WT or BD mutant PBRM1 were plated on day 0 and cells were harvested on designated time points for analysis. A designation of **** $P < 0.0001$ (paired Student $t$-test) for measurements at day 11. Error bars represent s.d. $n = 4$. (**E**) (left) Representative immunoblot of PBRM1 (PBAF) and ARID1A (cBAF) elution by sequential salt extraction (SSE) in Caki2 cells with WT PBRM1 and PBRM1 mutants. (right) Analysis of binding affinity to chromatin by SSE of PBRM1 in the BD mutants indicated by the percentage of PBRM1 eluted at increasing NaCl concentrations. $n = 4$ independent biological replicates. A designation of * $P < 0.05$ (paired Student $t$-test). Error bars represent s.d.

PBAF-specific subunits, such as ARID2, elute with a similar salt concentration as cBAF-specific subunits, such as ARID1A (42), supporting a similar affinity with chromatin. However, upon exogenous expression of PBRM1, other PBAF-specific subunits elute with slightly higher NaCl concentrations, indicating that PBRM1 enhances PBAF chromatin binding affinity. Here we observe a similar increase in the salt concentration required to elute WT PBRM1 compared to ARID1A (Figure 5E). However, the PBRM1 BD2 (SKY) and BD4 (KRK) mutants both elute with lower salt concentrations than WT PBRM1; this loss in binding affinity is similar to what we previously observed with alanine mutants of the acetyl-lysine binding asparagine in BD2 and BD4 (42). A decrease in binding affinity for the nucleic acid-binding mutants was consistent over multiple replicates, with a statistically significant difference in the percent of mutant PBRM1 eluted at 200 mM NaCl, compared to WT PBRM1 (Figure 5E). Re-expression of the PBRM1 BD2 SKY mutant has a SSE profile similar to cBAF (ARID1A) or PBAF without PBRM1 (71), while re-expression of the BD4 KRK mutant has an intermediate SSE profile. Considering the more pronounced effect of the BD2 mutation, as well as the increased affinity and selectivity for RNA observed for BD2 *in vitro*, we pursued additional genome-wide studies with the BD2 SKY PBRM1 mutant.

### BD2 nucleic acid binding residues contributes to PBRM1-mediated PBAF localization

To define how RNA-binding residue mutations in BD2 of PBRM1 affect PBAF function genome-wide, we performed ChIP-seq with PHF10, a core subunit of PBAF. To normalize the samples and control for variable IP efficiency, we included 5% of spike-in mouse chromatin into our samples. The spike-in chromatin was from a previous PHF10 ChIP-seq experiment in mouse NMuMG cells (unpublished data). Using 30 high confidence peaks from the mouse ChIP-seq analysis (Supplementary Figure S19a), we calculated the enrichment across these sites for each Caki2 ChIP (Supplementary Figure S19b) and normalized the human data by downsampling sequencing reads accordingly. Using MACS for peak calling, we identified 1393, 1803 and 1631 peaks in Vector, WT and SKY cell lines respectively. Consistent with reported PBAF ChIP-seq datasets, PHF10 peaks are often localized at promoters, although a significant number of PHF10 peaks were also associated with intergenic regions (Figure 6B). Using a combined dataset of PHF10 peaks identified from all three cell lines, we used metagene analysis to determine the average PHF10 enrichment across cell lines. The addition of PBRM1 increased average PHF10 enrichment slightly compared to empty vector, while the addition of BD2 SKY mutant PBRM1 did not (Figure 6A). While the overall ChIP signal was lower, the same trend was observed in a second biological replicate (Supplementary Figure S19c). To evaluate how the SKY mutation affects BD2 function, we wished to specifically evaluate PHF10 binding at H3K14ac sites. To do this, we performed ChIP-seq for H3K14ac in Caki2 cells with a spike-in panel of recombinant nucleosomes containing a variety of histone acetylation modifications. The H3K14ac antibody almost exclusively enriched nucleosomes containing H3K14ac and H3tetraAc (Supplementary Figure S19d), validating the specificity of the antibody. We identified 10,000–20,000 peaks for each ChIP (Supplementary Figure S19e), with a majority of peaks at promoters (Supplementary Figure S19f). The H3K14ac peaks identified from each cell line overlap, and have similar overall enrichment, as determined using the spike-in nucleosomes (Supplementary Figure S19d). Therefore, any difference in PHF10 enrichment is not due to differences in H3K14ac levels between the cell lines. We identified ∼600 overlapping peaks from the PHF10 and H3K14ac ChIP-seq in Caki2 cells expressing WT PBRM1 (Figure 6C). H3K14ac and PHF10 enrichment at these sites was almost exclusively at promoters (Figure 6D). At these binding sites, PBRM1 re-expression robustly increased PHF10 ChIP signal compared to vector control, while re-expression of the BD2 mutant PBRM1 (SKY) slightly decreases PHF10 enrichment (Figure 6E), which was also observed in the second biological replicate (Supplementary Figure S19g). Many of these promoters are at genes induced with PBRM1 re-expression in Caki2 (61,70), such as EGLN1, FGF12, IGFBP7, NID1, and FAM110C (Figure 6F, Supplementary Figure S19h). This implies that BD2 nucleic acid binding is important for association of PBAF to H3K14ac-marked promoters of tumor suppressive genes in Caki2 cells.

### PBRM1 nucleic acid binding residues are important for RNA binding in cells

To further determine whether the growth phenotype and chromatin binding properties observed for the PBRM1 mutants is related to RNA binding, we established whether full-length PBRM1 directly associates with RNA in cells using a crosslinking immunoprecipitation (CLIP) assay with $^{32}$P radiolabeled RNA. As a positive control, immunoprecipitation of hnRNP a 37 kDa RNA-binding protein, was included. Immunoprecipitation of the exogenously expressed PBRM1 under denaturing conditions with an antibody against V5 (Supplementary Figure S20a) reveals specific labelling of RNA at the same molecular weight only in cells expressing PBRM1 (Figure 7A, Supplementary Figure S20b). In comparison, PBRM1 with mutations in BD2 (SKY) or BD4 (KRK) have significantly reduced $^{32}$P labeling upon IP, indicating that the mutations decrease association with RNA in cells (Figure 7A, Supplementary Figure S20b). While both mutants displayed decreased PBRM1 RNA association, the mutations in BD2 (SKY) appeared to completely abrogate RNA association, while some labeling was still evident for the BD4 (KRK) mutant. Therefore, we focused on BD2 and performed CLIP-seq with WT PBRM1 and BD2 mutant PBRM1 to identify the RNAs that bind to PBRM1.

We generated CLIP-seq libraries using V5 IP in Caki2 with vector control (2 replicates and 1 input), Caki2 with WT PBRM1 re-expression (1 replicate and 1 input), and Caki2 with BD2 mutant PBRM1 (SKY) re-expression (2 replicates). Overall RNA yields were low; however, we were able to identify sites of enrichment in the CLIP-seq sequencing data. Using input samples as controls, we identified more peaks in the WT PBRM1 IP (105,000) compared to vector control (65,000 and 80,000) or SKY PBRM1

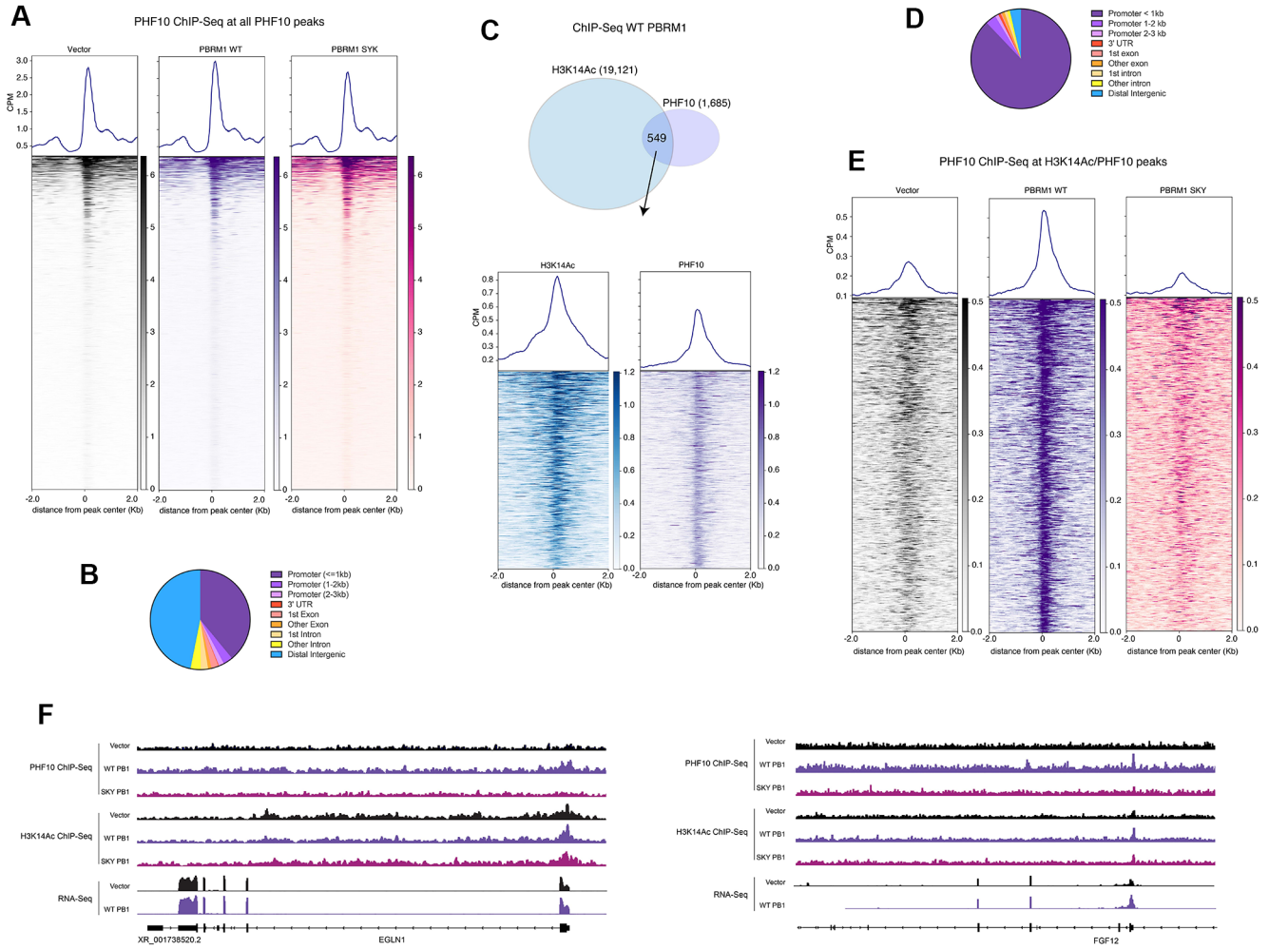


**Figure 6.** PBAF and H3K14ac ChIP-seq in Caki2 cells. (**A**) Heat map and metagene analysis at the combined PHF10 peaks from all Caki2 cells. Enrichment at these peaks is calculated for PHF10 ChIP-seq in Caki2 cells expressing vector control, WT PBRM1 or PBRM1 with BD2 SKY mutation. (**B**) Peak annotation for the combined PHF10 ChIP-seq peaks across cell lines (**C**) (top) Venn overlap of peaks from H3K14ac and PHF10 ChIP-seq in Caki2 cells expressing WT PBRM1. (bottom) Heat map and metagene analysis at the PHF10 and H3K14ac overlapping ChIP-seq peaks. Enrichment at these peaks is calculated for H3K14ac and PHF10 ChIP-seq in Caki2 cells expressing WT PBRM1. (**D**) Peak annotation for the overlapping PHF10 and H3K14ac ChIP-seq peaks from (C). (**E**) Heat map and metagene analysis at overlapping peaks from H3K14ac and PHF10 ChIP-seq represented in (C). Enrichment at these peaks is calculated for PHF10 ChIP-seq in Caki2 cells expressing vector control, WT PBRM1 or PBRM1 with BD2 SKY mutation. (**F**) IGV tracks for ChIP-seq and RNA-Seq enrichment at EGLN1 and FGF12 gene loci in Caki2 cells. RNA-seq data is from (61).

(86,000 and 93,000); however, the majority of peaks in all three cell lines overlap, indicating nonspecific RNA binding from the IP (Supplementary Figure S20c). We next performed peak calling between CLIP samples and identified 7094 peaks in WT PBRM1 CLIP compared to vector CLIP, and 4477 in WT PBRM1 CLIP compared to SKY PBRM1 CLIP. We focused on the intersection of these peaks (3165) for further analysis (Figure 7B). Several hundred of these CLIP peaks were associated with genes with PHF10 ChIP peaks at their promoters; however, very few PBRM1 CLIP-seq peaks were found in promoters where PHF10 binds. Instead, the majority of CLIP enrichment was found in introns or intergenic regions (Figure 7C). CLIP signal was found in the intronic regions of genes regulated by PBRM1 (Figure 7D), which could support a function for PBRM1 in binding mRNA *in cis* to facilitate transcription. In addition, many CLIP peaks were associated with ncRNA, including lncRNA, antisenseRNA and miRNA, (Supplementary Figure S20d), which could indicate a role for ncRNA in regulating PBRM1's chromatin binding and activity *in trans*. In addition, many sites with both PHF10 binding and CLIP binding are associated with antisense RNA, which could facilitate or inhibit transcription of the associated mRNA (Figure 7E) (74). Further work is needed to better validate and quantitate the specific RNAs bound to PBRM1 and elucidate how individual RNAs facilitate PBRM1 chromatin binding and PBAF remodeling function.

## DISCUSSION

In this study, we show that PBRM1 BD2, BD3, BD4 and BD5 bind to nucleic acids. We find that BD2 and BD4 preferentially bind to RNA over DNA *in vitro*, selectively associating with double-stranded RNA elements. The overall

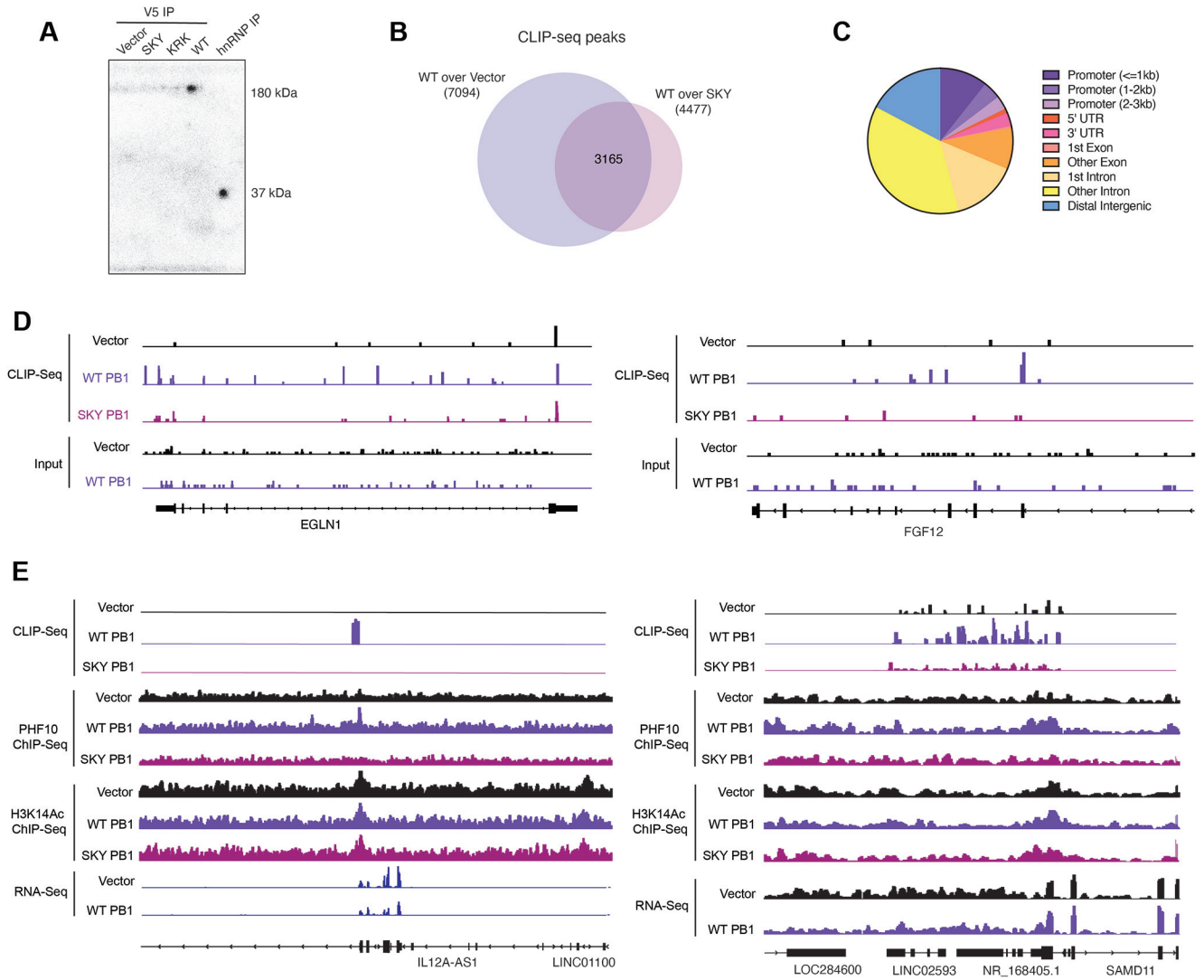


**Figure 7.** Crosslinking immunoprecipitation (CLIP) in Caki2 cells. (**A**) Phosphorimage of $^{32}$P-labeled immunoprecipitations of exogenous V5-tagged WT PBRM1 and mutants, as well as positive control hnRNPA1 from UV-crosslinked Caki2 cells. (**B**) Venn overlap of peaks from V5 CLIP-seq from UV-crosslinked Caki2 cells. Peaks are called for V5 IP from Caki2 cells expressing WT PBRM1 compared to Caki2 cells with empty vector or V5 IP from Caki2 cells expressing WT PBRM1 compared to Caki2 cells with BD2 SKY mutant. (**C**) Peak annotation for the overlapping peaks designated in (B). (**D**) IGV tracks for CLIP-seq enrichment at EGLN1 and FGF12 gene loci in Caki2 cells. (**E**) IGV tracks for CLIP-seq, ChIP-seq and RNA-Seq enrichment at ncRNA loci in Caki2 cells. RNA-seq data is from (61).

affinity and selectivity of BD2 with RNA is higher as compared to BD4. Notably, for both BDs the interaction with RNA leads to an enhanced affinity for acetylated histone tails.

In recent years, a number of known histone reader domains have been identified to also associate with DNA and/or RNA (75). This includes a subset of BDs, namely BRDT BD1 with DNA, BRG1/BRM BD with DNA, and BRD4 BD1 and BD2 with RNA (45–48). The molecular mechanism of association has been explored for the BRDT BD1 (45) and the BRG1/BRM BD (46,48) while the mechanism of BRD4 BD association with RNA is not yet known. For the BRG1/BRM BD the binding pocket spans the αA helix, ZA loop and very N-terminal end of the αZ helix (46,48) While less completely defined, the BRDT BD1 DNA binding pocket includes the αZ helix (45). Here we found that RNA binds BD4 in a region N-terminal to αZ as well as in αZ, and C-terminal to αC and in αC. On the other hand, the BD2 RNA binding pocket is mainly located in the αC and αB helices, as well as the BC and ZA loops. While DNA binds with lower affinity to both BD2 and BD4, the binding pockets are nearly identical to that seen for RNA. Thus, while the acetyl lysine binding pocket is well conserved amongst BDs, the nucleic acid binding pockets characterized to date vary in their sequence composition and positioning on the BD. The majority align along a face of the alpha helical bundle and are comprised of a charged patch rich in arginine and lysine, whereas recently BRD4 BD2 was shown to bind DNA using a pocket largely overlapping with the acetyl-lysine binding pocket. In addition, adjacent motifs such as the AT-hooks and intrinsically disordered linkers can contribute to the DNA binding (51,62,76,77).

It remains to be determined what the functional effect of enhanced histone tail binding upon RNA association is. The observation is in line with a previous study on BRD4 (47), where interaction of the BDs with an enhancer RNA were found to augment the pull-down of H3K27ac peptides. In the case of BRD4 it was proposed that this facilitated the cis stabilization at H3K27ac marked enhancers. A similar mechanism could be envisioned here with PBRM1 being stabilized at H3K14ac marked promoters upon binding to nascent transcripts. However, other mechanisms are also possible, such as association with lncRNA or asRNA. Additional studies are needed to fully elucidate the mechanisms of BD function. It is interesting that we did not observe an increase in affinity of BD4 for histone tails when bound to DNA, as BRG1/hBRM association with DNA was also not seen to enhance the affinity for histone tails. Though this suggests this could be an effect unique to BD association with RNA, more work is needed to fully understand this.

SWI/SNF subunits have previously been shown to interact with long non-coding RNAs (lncRNAs) (78–88). Interaction with lncRNAs can have a number of functional consequences including inhibition of activity by acting as a decoy, promoting activity through chromatin targeting or allosteric activation, or facilitating complex stability (89,90). While our results are consistent with a targeting or stability model, further studies are needed to determine the mechanism by which the RNA binding activity of the PBRM1 BDs is functioning *in vivo*. It should also be noted that while RNA is selected for *in vitro* under conditions of equal size and concentration, the relative importance of RNA versus DNA association in cells is not yet clear and is quite likely context dependent. Future studies are needed to understand the interplay between RNA, DNA and histone binding, and the cooperative action of all six BDs in PBAF activity.

Our data reveal that mutation of the nucleic acid binding pocket decreases PBRM1 affinity for chromatin and inhibition of Caki2 renal carcinoma cell proliferation. While the majority of PBRM1 mutations in renal cancers result in loss of protein expression, a subset of PBRM1-mutant tumors (∼15%) have missense mutations that cluster across the bromodomains. From the COSMIC database of somatic mutations in cancer, several missense mutations in the residues responsible for nucleic acid binding in both BD2 (S275L, Y28N, Y28C(2 patients), Y28F) and BD4 (K511E, and R512K) have been identified in patient tumors, with additional mutations in surrounding amino acids that may also affect nucleic acid binding (91). How these specific mutations found in patients affect nucleic binding and PBRM1 function remains to be elucidated.

## DATA AVAILABILITY

Chemical shift data were deposited to the BMRB with deposition numbers are 51326 and 51329. Sequencing data (ChIP-seq and CLIP-seq) were deposited to GEO with accession GSE221620. All other data is available upon reasonable request.

## SUPPLEMENTARY DATA

Supplementary Data are available at NAR Online.


## ACKNOWLEDGEMENTS

We would like to thank Drs David N.M. Jones and Chris Ptak for assistance with NMR, Drs Brian Wimberly and Quentin Vicens for discussions regarding RNA construct design. Thanks to the members of the Musselman laboratory as well as Drs Nicholas Schnicker and Zhen Xu for valuable discussions regarding this project. Thanks to Dr Aktan Alpsoy for assistance with cloning.

## FUNDING

Holden Comprehensive Cancer Center at the University of Iowa; National Cancer Institute Award [P30CA086862]; work in the Musselman lab is supported by the NIH [R35GM128705]; work in the Dykhuizen lab is supported by NIH [U01CA207532]; S.S. was supported by the Ross-Lynn Research Scholar Award administered through the Purdue College of Pharmacy; Genomics Core from the Purdue Center for Cancer Research, NIH grant [P30 CA023168]; work in the Vögeli lab is supported by the NIH [R01GM130694]; S.M.D.S. was funded in part by Graduate College of the University of Iowa; operation of the NMR spectrometers was supported by NIH grants [P30 CA046934 and S10 OD025020-01]. Funding for open access charge: NIH funds.

*Conflict of interest statement.* None declared.


## REFERENCES


1. Olins,D.E. and Olins,A.L. (2003) Chromatin history: our view from the bridge. *Nat. Rev. Mol. Cell Bio.*, **4**, 809–814.
2. Luger,K., Dechassa,M.L. and Tremethick,D.J. (2012) New insights into nucleosome and chromatin structure: an ordered state or a disordered affair? *Nat. Rev. Mol. Cell Bio.*, **13**, 436–447.
3. Luger,K., Mäder,A.W., Richmond,R.K., Sargent,D.F. and Richmond,T.J. (1997) Crystal structure of the nucleosome core particle at 2.8 Å resolution. *Nature*, **389**, 251–260.
4. Bouzoune,K. and Kingston,R.E. (2013) Assembly, remodelled. *Elife*, **2**, e00863.
5. Hargreaves,D.C. and Crabtree,G.R. (2011) ATP-dependent chromatin remodeling: genetics, genomics and mechanisms. *Cell Res.*, **21**, 396–420.
6. Zentner,G.E. and Henikoff,S. (2013) Regulation of nucleosome dynamics by histone modifications. *Nat. Struct. Mol. Biol.*, **20**, 259–266.
7. Han,P. and Chang,C.-P. (2015) Long non-coding RNA and chromatin remodeling. *Rna Biol.*, **12**, 1094–1098.
8. Tang,Y., Wang,J., Lian,Y., Fan,C., Zhang,P., Wu,Y., Li,X., Xiong,F., Li,X., Li,G. *et al.* (2017) Linking long non-coding RNAs and SWI/SNF complexes to chromatin remodeling in cancer. *Mol. Cancer*, **16**, 42.
9. Neigeborn,L. and Carlson,M. (1984) Genes affecting the regulation of SUC2 gene expression by glucose repression in *Saccharomyces cervisiae*. *Genetics*, **108**, 845–858.
10. Wang,W., Chi,T., Xue,Y., Zhou,S., Kuo,A. and Crabtree,G.R. (1998) Architectural DNA binding by a high-mobility-group/kinesin-like subunit in mammalian SWI/SNF-related complexes. *Proc. Natl. Acad Sci. U.S.A.*, **95**, 492–498.
11. Wang,W., Xue,Y., Zhou,S., Kuo,A., Cairns,B.R. and Crabtree,G.R. (1996) Diversity and specialization of mammalian SWI/SNF complexes. *Gene Dev.*, **10**, 2117–2130.
12. Wang,W., Côté,J., Xue,Y., Zhou,S., Khavari,P.A., Biggar,S.R., Muchardt,C., Kalpana,G.V., Goff,S.P., Yaniv,M. *et al.* (1996) Purification and biochemical heterogeneity of the mammalian SWI-SNF complex. *EMBO J.*, **15**, 5370–5382.
13. Nie,Z., Xue,Y., Yang,D., Zhou,S., Deroo,B.J., Archer,T.K. and Wang,W. (2000) A specificity and targeting subunit of a human

SWI/SNF family-related chromatin-remodeling complex. *Mol. Cell. Biol.*, **20**, 8879–8888.
14. Xue,Y., Canman,J.C., Lee,C.S., Nie,Z., Yang,D., Moreno,G.T., Young,M.K., Salmon,E.D. and Wang,W. (2000) The human SWI/SNF-B chromatin-remodeling complex is related to yeast Rsc and localizes at kinetochores of mitotic chromosomes. *Proc. Natl. Acad. Sci. U.S.A.*, **97**, 13015–13020.
15. Alpsoy,A. and Dykhuizen,E.C. (2018) Glioma tumor suppressor candidate region gene 1 (GLTSCR1) and its paralog GLTSCR1-like form SWI/SNF chromatin remodeling subcomplexes. *J. Biol. Chem.*, **293**, 3892–3903.
16. Mashtalir,N., D'Avino,A.R., Michel,B.C., Luo,J., Pan,J., Otto,J.E., Zullow,H.J., McKenzie,Z.M., Kubiak,R.L., Pierre,R.St. *et al.* (2018) Modular organization and assembly of SWI/SNF family chromatin remodeling complexes. *Cell*, **175**, 1272–1288.
17. Yan,Z., Cui,K., Murray,D.M., Ling,C., Xue,Y., Gerstein,A., Parsons,R., Zhao,K. and Wang,W. (2005) PBAF chromatin-remodeling complex requires a novel specificity subunit, BAF200, to regulate expression of selective interferon-responsive genes. *Gene Dev*, **19**, 1662–1667.
18. Kaeser,M.D., Aslanian,A., Dong,M.-Q., Yates,J.R. and Emerson,B.M. (2008) BRD7, a novel PBAF-specific SWI/SNF subunit, is required for target gene activation and repression in embryonic stem cells. *J. Biol. Chem.*, **283**, 32254–32263.
19. Kadoch,C., Hargreaves,D.C., Hodges,C., Elias,L., Ho,L., Ranish,J. and Crabtree,G.R. (2013) Proteomic and bioinformatic analysis of mammalian SWI/SNF complexes identifies extensive roles in human malignancy. *Nat. Genet.*, **45**, 592–601.
20. Brownlee,P.M., Chambers,A.L., Oliver,A.W. and Downs,J.A. (2012) Cancer and the bromodomains of BAF180. *Biochem. Soc. Trans.*, **40**, 364–369.
21. Varela,I., Tarpey,P., Raine,K., Huang,D., Ong,C.K., Stephens,P., Davies,H., Jones,D., Lin,M.-L., Teague,J. *et al.* (2011) Exome sequencing identifies frequent mutation of the SWI/SNF complex gene PBRM1 in renal carcinoma. *Nature*, **469**, 539–542.
22. Gu,Y.-F., Cohn,S., Christie,A., McKenzie,T., Wolff,N., Do,Q.N., Madhuranthakam,A.J., Pedrosa,I., Wang,T., Dey,A. *et al.* (2017) Modeling renal cell carcinoma in mice: bap1 and Pbrm1 inactivation drive tumor grade. *Cancer Discov.*, **7**, 900–917.
23. Espana-Agusti,J., Warren,A., Chew,S.K., Adams,D.J. and Matakidou,A. (2017) Loss of PBRM1 rescues VHL dependent replication stress to promote renal carcinogenesis. *Nat. Commun.*, **8**, 2026.
24. Nargund,A.M., Pham,C.G., Dong,Y., Wang,P.I., Osmangeyoglu,H.U., Xie,Y., Aras,O., Han,S., Oyama,T., Takeda,S. *et al.* (2017) The SWI/SNF protein PBRM1 restrains VHL-loss-driven clear cell renal cell carcinoma. *Cell Rep.*, **18**, 2893–2906.
25. Carril-Ajuria,L., Santos,M., Roldán-Romero,J.M., Rodriguez-Antona,C. and Velasco,G.de (2019) Prognostic and predictive value of PBRM1 in clear cell renal cell carcinoma. *Cancers*, **12**, 16.
26. Pan,D., Kobayashi,A., Jiang,P., Andrade,L.F.de, Tay,R.E., Luoma,A.M., Tsoucas,D., Qiu,X., Lim,K., Rao,P. *et al.* (2018) A major chromatin regulator determines resistance of tumor cells to T cell–mediated killing. *Science*, **359**, 770–775.
27. Mota,S.T.S., Vecchi,L., Zóia,M.A.P., Oliveira,F.M., Alves,D.A., Dornelas,B.C., Bezerra,S.M., Andrade,V.P., Maia,Y.C.P., Neves,A.F. *et al.* (2019) New insights into the role of polybromo-1 in prostate cancer. *Int. J. Mol. Sci.*, **20**, 2852.
28. Kakarougkas,A., Ismail,A., Chambers,A.L., Riballo,E., Herbert,A.D., Künzel,J., Löbrich,M., Jeggo,P.A. and Downs,J.A. (2014) Requirement for PBAF in transcriptional repression and repair at DNA breaks in actively transcribed regions of chromatin. *Mol. Cell*, **55**, 723–732.
29. Gao,W., Li,W., Xiao,T., Liu,X.S. and Kaelin,W.G. (2017) Inactivation of the PBRM1 tumor suppressor gene amplifies the HIF-response in VHL−/− clear cell renal carcinoma. *Proc. Natl. Acad. Sci. U.S.A.*, **114**, 1027–1032.
30. Chowdhury,B., Porter,E.G., Stewart,J.C., Ferreira,C.R., Schipma,M.J. and Dykhuizen,E.C. (2016) PBRM1 regulates the expression of genes involved in metabolism and cell adhesion in renal clear cell carcinoma. *PLoS One*, **11**, e0153718.
31. Porter,E.G., Dhiman,A., Chowdhury,B., Carter,B.C., Lin,H., Stewart,J.C., Kazemian,M., Wendt,M.K. and Dykhuizen,E.C. (2019) PBRM1 regulates stress response in epithelial cells. *Iscience*, **15**, 196–210.
32. Hagiwara,M., Fushimi,A., Yamashita,N., Bhattacharya,A., Rajabi,H., Long,M.D., Yasumizu,Y., Oya,M., Liu,S. and Kufe,D. (2021) MUC1-C activates the PBAF chromatin remodeling complex in integrating redox balance with progression of human prostate cancer stem cells. *Oncogene*, **40**, 4930–4940.
33. Thompson,M. (2009) Polybromo-1: the chromatin targeting subunit of the PBAF complex. *Biochimie*, **91**, 309–319.
34. Thomas,J.O. and Travers,A.A. (2001) HMG1 and 2, and related 'architectural' DNA-binding proteins. *Trends Biochem. Sci*, **26**, 167–174.
35. Štros,M., Launholt,D. and Grasser,K.D. (2007) The HMG-box: a versatile protein domain occurring in a wide variety of DNA-binding proteins. *Cell. Mol. Life Sci.*, **64**, 2590.
36. Yang,N. and Xu,R.-M. (2012) Structure and function of the BAH domain in chromatin biology. *Crit. Rev. Biochem. Mol.*, **48**, 211–221.
37. Karki,M., Jangid,R.K., Anish,R., Seervai,R.N.H., Bertocchio,J.-P., Hotta,T., Msaouel,P., Jung,S.Y., Grimm,S.L., Coarfa,C. *et al.* (2021) A cytoskeletal function for PBRM1 reading methylated microtubules. *Sci. Adv.*, **7**, eabf2866.
38. Zaware,N. and Zhou,M.-M. (2019) Bromodomain biology and drug discovery. *Nat. Struct. Mol. Biol.*, **26**, 870–879.
39. Filippakopoulos,P., Picaud,S., Mangos,M., Keates,T., Lambert,J.-P., Barsyte-Lovejoy,D., Felletar,I., Volkmer,R., Müller,S., Pawson,T. *et al.* (2012) Histone recognition and large-scale structural analysis of the human bromodomain family. *Cell*, **149**, 214–231.
40. Zeng,L. and Zhou,M.-M. (2002) Bromodomain: an acetyl-lysine binding domain. *FEBS Lett.*, **513**, 124–128.
41. Liao,L., Alicea-Velázquez,N.L., Langbein,L., Niu,X., Cai,W., Cho,E., Zhang,M., Greer,C.B., Yan,Q., Cosgrove,M.S. *et al.* (2019) High affinity binding of H3K14ac through collaboration of bromodomains 2, 4 and 5 is critical for the molecular and tumor suppressor functions of PBRM1. *Mol. Oncol.*, **13**, 811–828.
42. Porter,E.G. and Dykhuizen,E.C. (2017) Individual bromodomains of polybromo-1 contribute to chromatin association and tumor suppression in clear cell renal carcinoma. *J. Biol. Chem.*, **292**, 2601–2610.
43. Slaughter,M.J., Shanle,E.K., McFadden,A.W., Hollis,E.S., Suttle,L.E., Strahl,B.D. and Davis,I.J. (2018) PBRM1 bromodomains variably influence nucleosome interactions and cellular function. *J. Biol. Chem.*, **293**, 13592–13603.
44. Cai,W., Su,L., Liao,L., Liu,Z.Z., Langbein,L., Dulaimi,E., Testa,J.R., Uzzo,R.G., Zhong,Z., Jiang,W. *et al.* (2019) PBRM1 acts as a p53 lysine-acetylation reader to suppress renal tumor growth. *Nat. Commun.*, **10**, 5800.
45. Miller,T.C.R., Simon,B., Rybin,V., Grötsch,H., Curtet,S., Khochbin,S., Carlomagno,T. and Müller,C.W. (2016) A bromodomain–DNA interaction facilitates acetylation-dependent bivalent nucleosome recognition by the BET protein BRDT. *Nat. Commun.*, **7**, 13855.
46. Morrison,E.A., Sanchez,J.C., Ronan,J.L., Farrell,D.P., Varzavand,K., Johnson,J.K., Gu,B.X., Crabtree,G.R. and Musselman,C.A. (2017) DNA binding drives the association of BRG1/hBRM bromodomains with nucleosomes. *Nat. Commun.*, **8**, 16080.
47. Rahnamoun,H., Lee,J., Sun,Z., Lu,H., Ramsey,K.M., Komives,E.A. and Lauberth,S.M. (2018) RNAs interact with BRD4 to promote enhanced chromatin engagement and transcription activation. *Nat. Struct. Mol. Biol.*, **25**, 687–697.
48. Sanchez,J.C., Zhang,L., Evoli,S., Schnicker,N.J., Nunez-Hernandez,M., Yu,L., Wereszczynski,J., Pufall,M.A. and Musselman,C.A. (2020) The molecular basis of selective DNA binding by the BRG1 AT-hook and bromodomain. *Biochim. Biophys. Acta*, **1863**, 194566.
49. Daneshvar,K., Ardehali,M.B., Klein,I.A., Hsieh,F.-K., Kratkiewicz,A.J., Mahpour,A., Cancelliere,S.O.L., Zhou,C., Cook,B.M., Li,W. *et al.* (2020) lncRNA DIGIT and BRD3 protein form phase-separated condensates to regulate endoderm differentiation. *Nat. Cell Biol.*, **22**, 1211–1222.
50. Pistoni,M., Rossi,T., Donati,B., Torricelli,F., Polano,M. and Ciarrocchi,A. (2021) Long noncoding RNA NEAT1 acts as a molecular switch for BRD4 transcriptional activity and mediates

repression of BRD4/WDR5 target genes. *Mol. Cancer Res.*, **19**, 799–811.
51. Kalra,P., Zahid,H., Ayoub,A., Dou,Y. and Pomerantz,W.C.K. (2022) Alternative mechanisms for DNA engagement by BET bromodomain-containing proteins. *Biochemistry*, **61**, 1260–1272.
52. Dyer,P.N., Edayathumangalam,R.S., White,C.L., Bao,Y., Chakravarthy,S., Muthurajan,U.M. and Luger,K. (2003) Reconstitution of nucleosome core particles from recombinant histones and DNA. *Methods Enzymol.*, **375**, 23–44.
53. Cavanagh,J., Fairbrother,W.J., Skelton,N.J., PalmerIII,A.G. and Rance,M. (2010) In: *Protein NMR Spectroscopy: Principles and Practice 2nd edition*. Elsevier Science.
54. Delaglio,F., Grzesiek,S., Vuister,G.W., Zhu,G., Pfeifer,J. and Bax,A. (1995) NMRPipe: a multidimensional spectral processing system based on UNIX pipes. *J. Biomol. NMR*, **6**, 277–293.
55. Vranken,W.F., Boucher,W., Stevens,T.J., Fogh,R.H., Pajon,A., Llinas,M., Ulrich,E.L., Markley,J.L., Ionides,J. and Laue,E.D. (2005) The CCPN data model for NMR spectroscopy: development of a software pipeline. *Proteins Struct. Funct. Bioinform.*, **59**, 687–696.
56. Ying,J., Delaglio,F., Torchia,D.A. and Bax,A. (2017) Sparse multidimensional iterative lineshape-enhanced (SMILE) reconstruction of both non-uniformly sampled and conventional NMR data. *J. Biomol. NMR*, **68**, 101–118.
57. Williamson,M.P. (2013) Using chemical shift perturbation to characterise ligand binding. *Prog. Nucl. Mag. Res. Sp.*, **73**, 1–16.
58. Liu,H., Patel,M.R., Prescher,J.A., Patsialou,A., Qian,D., Lin,J., Wen,S., Chang,Y.-F., Bachmann,M.H., Shimono,Y. *et al.* (2010) Cancer stem cells from human breast tumors are involved in spontaneous metastases in orthotopic mouse models. *Procc. Natl. Acad. Sci. U.S.A.*, **107**, 18115–18120.
59. Porter,E.G., Connelly,K.E. and Dykhuizen,E.C. (2017) Sequential salt extractions for the analysis of bulk chromatin binding properties of chromatin modifying complexes. *J. Vis. Exp.*, **128**, 55369.
60. Tian,B., Yang,J. and Brasier,A.R. (2011) Transcriptional regulation, methods and protocols. *Methods Mol. Biol.*, **809**, 105–120.
61. Chowdhury,B., Porter,E.G., Stewart,J.C., Ferreira,C.R., Schipma,M.J. and Dykhuizen,E.C. (2016) PBRM1 regulates the expression of genes involved in metabolism and cell adhesion in renal clear cell carcinoma. *PLoS One*, **11**, e0153718.
62. Morrison,E.A., Sanchez,J.C., Ronan,J.L., Farrell,D.P., Varzavand,K., Johnson,J.K., Gu,B.X., Crabtree,G.R. and Musselman,C.A. (2017) DNA binding drives the association of BRG1/hBRM bromodomains with nucleosomes. *Nat. Commun.*, **8**, 16080.
63. Shen,Y., Delaglio,F., Cornilescu,G. and Bax,A. (2009) TALOS+: a hybrid method for predicting protein backbone torsion angles from NMR chemical shifts. *J. Biomol. NMR*, **44**, 213–223.
64. Marsh,J.A., Singh,V.K., Jia,Z. and Forman-Kay,J.D. (2006) Sensitivity of secondary structure propensities to sequence differences between alpha- and gamma-synuclein: implications for fibrillation. *Protein Sci. Publ. Protein Soc.*, **15**, 2795–2804.
65. Nargund,A.M., Pham,C.G., Dong,Y., Wang,P.I., Osmangeyoglu,H.U., Xie,Y., Aras,O., Han,S., Oyama,T., Takeda,S. *et al.* (2017) The SWI/SNF protein PBRM1 restrains VHL-loss-driven clear cell renal cell carcinoma. *Cell Rep.*, **18**, 2893–2906.
66. Espana-Agusti,J., Warren,A., Chew,S.K., Adams,D.J. and Matakidou,A. (2017) Loss of PBRM1 rescues VHL dependent replication stress to promote renal carcinogenesis. *Nat. Commun.*, **8**, 2026.
67. Gu,Y.-F., Cohn,S., Christie,A., McKenzie,T., Wolff,N., Do,Q.N., Madhuranthakam,A.J., Pedrosa,I., Wang,T., Dey,A. *et al.* (2017) Modeling renal cell carcinoma in mice: bap1 and Pbrm1 Inactivation drive tumor grade. *Cancer Discov.*, **7**, 900–917.
68. Lee,H., Dai,F., Zhuang,L., Xiao,Z.-D., Kim,J., Zhang,Y., Ma,L., You,M.J., Wang,Z. and Gan,B. (2016) BAF180 regulates cellular senescence and hematopoietic stem cell homeostasis through p21. *Oncotarget*, **7**, 19134–19146.
69. Murakami,A., Wang,L., Kalhorn,S., Schraml,P., Rathmell,W.K., Tan,A.C., Nemenoff,R., Stenmark,K., Jiang,B.-H., Reyland,M.E. *et al.* (2017) Context-dependent role for chromatin remodeling component PBRM1/BAF180 in clear cell renal cell carcinoma. *Oncogenesis*, **6**, e287.
70. Porter,E.G., Dhiman,A., Chowdhury,B., Carter,B.C., Lin,H., Stewart,J.C., Kazemian,M., Wendt,M.K. and Dykhuizen,E.C. (2019) PBRM1 regulates stress response in epithelial cells. *Iscience*, **15**, 196–210.
71. Porter,E.G. and Dykhuizen,E.C. (2017) Individual bromodomains of polybromo-1 contribute to chromatin association and tumor suppression in clear cell renal carcinoma. *J. Biol. Chem.*, **292**, 2601–2610.
72. Mashtalir,N., D'Avino,A.R., Michel,B.C., Luo,J., Pan,J., Otto,J.E., Zullow,H.J., McKenzie,Z.M., Kubiak,R.L., Pierre,R.S. *et al.* (2018) Modular organization and assembly of SWI/SNF family chromatin remodeling complexes. *Cell*, **175**, 1272–1288.
73. Yan,Z., Cui,K., Murray,D.M., Ling,C., Xue,Y., Gerstein,A., Parsons,R., Zhao,K. and Wang,W. (2005) PBAF chromatin-remodeling complex requires a novel specificity subunit, BAF200, to regulate expression of selective interferon-responsive genes. *Gene Dev*, **19**, 1662–1667.
74. Saberi,F., Kamali,M., Najafi,A., Yazdanparast,A. and Moghaddam,M.M. (2016) Natural antisense RNAs as mRNA regulatory elements in bacteria: a review on function and applications. *Cell. Mol. Biol. Lett.*, **21**, 6.
75. Weaver,T.M., Morrison,E.A. and Musselman,C.A. (2018) Reading more than histones: the prevalence of nucleic acid binding among reader domains. *Mol. J. Synth. Chem. Nat. Prod. Chem.*, **23**, 2614.
76. Lupo,B.E., Chu,P., Harms,M.J., Morrison,E.A. and Musselman,C.A. (2021) Evolutionary conservation of structural and functional coupling between the BRM AT-hook and bromodomain. *J. Mol. Biol.*, **433**, 166845.
77. Sanchez,J.C., Zhang,L., Evoli,S., Schnicker,N.J., Nunez-Hernandez,M., Yu,L., Wereszczynski,J., Pufall,M.A. and Musselman,C.A. (2020) The molecular basis of specific DNA binding by the BRG1 AT-hook and bromodomain. *Biochim. Biophys. Acta Gene Regul. Mech.*, **1863**, 194566.
78. Prensner,J.R., Iyer,M.K., Sahu,A., Asangani,I.A., Cao,Q., Patel,L., Vergara,I.A., Davicioni,E., Erho,N., Ghadessi,M. *et al.* (2013) The long noncoding RNA SChLAP1 promotes aggressive prostate cancer and antagonizes the SWI/SNF complex. *Nat. Genet.*, **45**, 1392–1398.
79. Lee,R.S. and Roberts,C.W.M. (2013) Linking the SWI/SNF complex to prostate cancer. *Nat. Genet.*, **45**, 1268–1269.
80. Wang,X., Gong,Y., Jin,B., Wu,C., Yang,J., Wang,L., Zhang,Z. and Mao,Z. (2014) Long non-coding RNA urothelial carcinoma associated 1 induces cell replication by inhibiting BRG1 in 5637 cells. *Oncol. Rep.*, **32**, 1281–1290.
81. Wang,S., Zhang,X., Yuan,Y., Tan,M., Zhang,L., Xue,X., Yan,Y., Han,L. and Xu,Z. (2015) BRG1 expression is increased in thoracic aortic aneurysms and regulates proliferation and apoptosis of vascular smooth muscle cells through the long non-coding RNA HIF1A-AS1 in vitro. *Eur. J. Cardiothorac.*, **47**, 439–446.
82. Wang,Y., He,L., Du,Y., Zhu,P., Huang,G., Luo,J., Yan,X., Ye,B., Li,C., Xia,P. *et al.* (2015) The long noncoding RNA lncTCF7 promotes self-renewal of human liver cancer stem cells through activation of Wnt signaling. *Cell Stem Cell*, **16**, 413–425.
83. Kawaguchi,T., Tanigawa,A., Naganuma,T., Ohkawa,Y., Souquere,S., Pierron,G. and Hirose,T. (2015) SWI/SNF chromatin-remodeling complexes function in noncoding RNA-dependent assembly of nuclear bodies. *Proc. Natl. Acad. Sci. U.S.A.*, **112**, 4304–4309.
84. Zhu,P., Wang,Y., Wu,J., Huang,G., Liu,B., Ye,B., Du,Y., Gao,G., Tian,Y., He,L. *et al.* (2016) LncBRM initiates YAP1 signalling activation to drive self-renewal of liver cancer stem cells. *Nat. Commun.*, **7**, 13608.
85. Hu,G., Gong,A.-Y., Wang,Y., Ma,S., Chen,X., Chen,J., Su,C.-J., Shibata,A., Strauss-Soukup,J.K., Drescher,K.M. *et al.* (2016) LincRNA-Cox2 promotes late inflammatory gene transcription in macrophages through modulating SWI/SNF-mediated chromatin remodeling. *J. Immunol.*, **196**, 2799–2808.
86. Liu,X., Lu,Y., Zhu,J., Liu,M., Xie,M., Ye,M., Li,M., Wang,S., Ming,Z., Tong,Q. *et al.* (2019) A long noncoding RNA, antisense IL-7, promotes inflammatory gene transcription through facilitating histone acetylation and switch/sucrose nonfermentable chromatin remodeling. *J. Immunol.*, **203**, 1548–1559.
87. Grossi,E., Raimondi,I., Goñi,E., González,J., Marchese,F.P., Chapaprieta,V., Martín-Subero,J.I., Guo,S. and Huarte,M. (2020) A lncRNA-SWI/SNF complex crosstalk controls transcriptional activation at specific promoter regions. *Nat. Commun.*, **11**, 936.
88. Leisegang,M.S., Fork,C., Josipovic,I., Richter,F.M., Preussner,J., Hu,J., Miller,M.J., Epah,J., Hofmann,P., Günther,S. *et al.* (2017)

Long noncoding RNA MANTIS facilitates endothelial angiogenic function. *Circulation*, **136**, 65–79.
89. Mallam,A.L., Sae-Lee,W., Schaub,J.M., Tu,F., Battenhouse,A., Jang,Y.J., Kim,J., Wallingford,J.B., Finkelstein,I.J., Marcotte,E.M. *et al.* (2019) Systematic Discovery of Endogenous Human Ribonucleoprotein Complexes. *Cell Rep.*, **29**, 1351–1368.
90. Guttman,M. and Rinn,J.L. (2012) Modular regulatory principles of large non-coding RNAs. *Nature*, **482**, 339–346.
91. Tate,J.G., Bamford,S., Jubb,H.C., Sondka,Z., Beare,D.M., Bindal,N., Boutselakis,H., Cole,C.G., Creatore,C., Dawson,E. *et al.* (2018) COSMIC: the catalogue of somatic mutations in cancer. *Nucleic Acids Res.*, **47**, D941–D947.